

# Manipulating Spin-Lattice Coupling in Layered Magnetic Topological Insulator Heterostructure *via* Interface Engineering

Sujan Maity,<sup>1</sup> Dibyendu Dey,<sup>2</sup> Anudeepa Ghosh,<sup>1</sup> Suvadip Masanta,<sup>3</sup> Binoy Krishna De,<sup>4</sup> Hemant Singh Kunwar,<sup>4</sup> Bikash Das,<sup>1</sup> Tanima Kundu,<sup>1</sup> Mainak Palit,<sup>1</sup> Satyabrata Bera,<sup>1</sup> Kapildeb Dolui,<sup>5</sup> Kenji Watanabe,<sup>6</sup> Takashi Taniguchi,<sup>7</sup> Liping Yu,<sup>2</sup> A Taraphder,<sup>8</sup> and Subhadeep Datta\*<sup>1</sup>

<sup>1</sup>*School of Physical Sciences, Indian Association for the Cultivation of Science,  
2A & 2B Raja S. C. Mullick Road, Jadavpur, Kolkata - 700032, India*

<sup>2</sup>*Department of Physics and Astronomy,  
University of Maine, Orono, ME 04469, USA*

<sup>3</sup>*Bose Institute, Department of Physics Main Campus 93/1,  
A. P. C. Road Kolkata - 700 009, India*

<sup>4</sup>*UGC-DAE Consortium for Scientific Research, Indore Centre,  
University Campus, Khandwa Road, Indore 452001*

<sup>5</sup>*Lomare Technolgies Limited, 6 London Street, London EC3R 7LP, United Kingdom*

<sup>6</sup>*Research Center for Functional Materials,  
National Institute for Materials Science, Tsukuba 305-0044, Japan*

<sup>7</sup>*International Center for Materials Nanoarchitectonics,  
National Institute for Materials Science, Tsukuba 305-0044, Japan*

<sup>8</sup>*Department of Physics, Indian Institute of Technology Kharagpur, W.B. 721302, India*

## Abstract

Induced magnetic order in a topological insulator (TI) can be realized either by depositing magnetic adatoms on the surface of a TI or engineering the interface with epitaxial thin film or stacked assembly of two-dimensional (2D) van der Waals (vdW) materials. Herein, we report the observation of spin-phonon coupling in the otherwise non-magnetic TI  $\text{Bi}_2\text{Te}_3$ , due to the proximity of  $\text{FePS}_3$  (an antiferromagnet (AFM),  $T_N \sim 120$  K), in a vdW heterostructure framework. Temperature-dependent Raman spectroscopic studies reveal deviation from the usual phonon anharmonicity originated from spin-lattice coupling at the  $\text{Bi}_2\text{Te}_3/\text{FePS}_3$  interface at/below 60 K in the peak position (self-energy) and linewidth (lifetime) of the characteristic phonon modes of  $\text{Bi}_2\text{Te}_3$  ( $106 \text{ cm}^{-1}$  and  $138 \text{ cm}^{-1}$ ) in the stacked heterostructure. The Ginzburg-Landau (GL) formalism, where the respective phonon frequencies of  $\text{Bi}_2\text{Te}_3$  couple to phonons of similar frequencies of  $\text{FePS}_3$  in the AFM phase, has been adopted to understand the origin of the hybrid magneto-elastic modes. At the same time, the reduction of characteristic  $T_N$  of  $\text{FePS}_3$  from 120 K in isolated flakes to 65 K in the heterostructure, possibly due to the interfacial strain, which leads to smaller Fe-S-Fe bond angles as corroborated by computational studies using density functional theory (DFT). Besides, inserting hexagonal boron nitride within  $\text{Bi}_2\text{Te}_3/\text{FePS}_3$  stacking regains the anharmonicity in  $\text{Bi}_2\text{Te}_3$ . Controlling interfacial spin-phonon coupling in stacked heterostructure can have potential application in surface code spin logic devices.

## INTRODUCTION

The realization of the quantum anomalous Hall effect (QAHE) and topological magneto-electric effect (TMAE) depends on the functional electronic interface between the (anti-)ferromagnet and topological insulator (TI) in the engineered heterostructure framework. Effect on Dirac cone-like surface state of TI due to hybridization and charge transfer across the interface and subsequent formation of an exchange gap due to proximity effects result in an efficient control over the exotic state [1]. Recently, a series of experiments on TIs doped with 3d transition metals [2–5] has led to the observation of broken time-reversal symmetry (TRS) and the consequent opening of a band gap in the surface band structure. Moreover, magnetically doped-TI shows current-induced giant spin-orbit torque (SOT) which in turn may result in ultra-low power memory and logic devices [6]. But still, the sample inhomogeneity and the formation of a disordered cluster in ferromag-

netically doped TIs, even with ppm level of doping concentration, restricts the anomalous Hall regime to one or two orders of magnitude less than the Curie-temperature ( $T_C \sim 30$  K for magnetically doped Bi-Sb alloy) [7]. However, in the interface-controlled magnetic heterostructure (*e.g.* Fe overlayer is deposited on TI), one may preserve long-range ferromagnetism at ambient temperature [8]. Even so, in this metallic FM-TI heterostructure, the possibility of alteration of the topological surface state due to intermixing with the bulk charge carriers, and most importantly, metallic iron film working as a short circuit on TI would impede future spintronic device applications. Furthermore, epitaxial integration (molecular beam epitaxy) of a high-quality thin film of topological insulator (*e.g.*  $\text{Bi}_2\text{Te}_3$ ,  $\text{Bi}_2\text{Se}_3$ ) on insulating magnetic substrate (*e.g.*  $\text{Y}_3\text{Fe}_5\text{O}_{12}$ , EuS), with slightest chemical reaction at the interface, can show AHE but limited to low temperature ( $\sim 22$  K for EuS) due to the choice of the magnet [9]. Even for antiferromagnets (AFM) exhibiting no macroscopic magnetization, while short-range interfacial exchange coupling [10] in the interface can be crucial for manipulating magnetic state, as reported in CrSb (AFM with  $T_N \sim 700$  K)/Cr-doped(Bi, Sb) $_2\text{Te}_3$  (FM with  $T_C \sim 35$  K) thin film superlattice [11], doping and heterostructure engineering checks the temperature scale close to 50 K. Also, the high sensitivity of the surface states of TI to air exposure puts a limit on the sample characterization and applicability.

For an atomically-flat interface with reasonable air-stability (see Supplementary Information Fig. S19), layered two-dimensional (2D) material-based van der Waals heterostructures (vdWh) are proving to be better to create proximity-induced effects in low-power electronic circuits [12]. For example, introducing graphene (Graphene / Europium oxide (EuO) [13], Graphene/ $\text{BiFeO}_3$  [14], Graphene/EuS [15], Graphene/yttrium-iron-garnet (YIG) [16]) with magnetic thin films may be used as an electrical read-out of the magnetic order. Moreover, modulation of interfacial spin texture and long-range exchange coupling mediated by magnetic order significantly enhances the transition temperature in the superlattice [13]. In fact, the net magnetic moment induced on graphene due to magnetic proximity ( $0.1 \mu_B$  per C atom) is nearly double that of Pt on magnetic insulator (MI), as reported in the x-ray magnetic circular dichroism (XMCD) studies [17]. In the case of vdW semiconductor-magnet heterostructure, or in other words, valley-spin related device consisting of layered transition metal dichalcogenide (TMDC), theoretical predictions have been made where an induced Zeeman field creates giant valley splitting ( $\sim 300$  meV) due to proximity effect in case of (i) ferromagnetic heterostructure in  $\text{MoTe}_2$ -EuO [18], and (ii) antiferromagnets as in  $\text{WS}_2$ -MnO(111) [19],  $\text{MoS}_2$ -CoO(111) [20] and TMD-CrI $_3$  [21]. As furtherance, the stacked all-2D assembly offers proximity-induced spin-texture with controlled magnetic anisotropy to-

gether with persistent magnetoresistance above transition temperature which has been reported in graphene - vdW FM ( $\text{Cr}_2\text{Ge}_2\text{Te}_6$  with  $T_C \sim 60$  K) heterostructure [22].

TI-MI heterostructures with vdW materials have been intensively studied using electronic transport measurements of micro/nano-electronic devices fabricated *via* lithography [23]. But, probing the contributions of each constituent layer in the stacking is difficult to conclude from conventional magnetoresistance measurements. Alternatively, Raman spectroscopy offers an indirect tool to detect characteristic phonon mode/s, elementary excitations (*e.g.* magnons), spin-phonon and electron-phonon coupling in 2D magnets (for example, in ferromagnets  $\text{Fe}_3\text{GeTe}_2$  [24],  $\text{CrSiTe}_3$  [25], and in antiferromagnets  $\text{FePS}_3$  [26]) and topological insulators ( $\text{Bi}_2\text{Te}_3$  [27],  $\text{Bi}_2\text{Se}_3$  [28]) in its few-atomic layer form. In particular, magnetic transition in *strictly-2D* magnets with magnetic anisotropy can easily be detected *via* spin-phonon coupling, as analyzed by Ghosh *et al.*[26] in case of  $\text{FePS}_3$  by marking the point of deviation (hardening or softening of phonon modes) in temperature-dependent phonon anharmonicity. Note that out of all predicted and experimentally verified 2D FMs and AFMs,  $\text{FePS}_3$ , an antiferromagnet ( $T_N \sim 120$  K in bulk), shows layer-thickness independent transition temperature [26, 29] which could be crucial for high-temperature applications keeping 2D nature of the heterostructure intact. Also, the pristine quality of less-strained micromanipulated structure with TI which provides low density of states (DOS) at the interface and the greater probability of hybridization with the electronic states from the overlying layered magnets, creates an ideal platform to study the material-specific modification *via* recognizing the Raman modes as a function of temperature. To the best of our knowledge, there are no reports to date that concerns Raman spectroscopic studies on proximity-induced magnetic order on TI in engineered vdW AFM-TI heterostructure.

Here, we present temperature-dependent Raman spectroscopic studies on *all-2D* topological insulator ( $\text{Bi}_2\text{Te}_3$ ) - antiferromagnet ( $\text{FePS}_3$ ) vdW heterostructure stacked on Si/SiO<sub>2</sub> substrate. With temperature (down to 5 K), we track all the characteristic phonon modes of (i)  $\text{FePS}_3$  which have previously been observed to demonstrate spin-phonon coupling ( $250\text{ cm}^{-1}$ ,  $280\text{ cm}^{-1}$  and  $380\text{ cm}^{-1}$ ), zone-folding (around  $105\text{ cm}^{-1}$ ), and magnon ( $120\text{ cm}^{-1}$ ), and (ii)  $\text{Bi}_2\text{Te}_3$  ( $106\text{ cm}^{-1}$  and  $138\text{ cm}^{-1}$ ), and analyze the data with the anharmonic phonon-decay model. We note that observed deviation from the usual phonon anharmonicity in peak position (self-energy) and linewidth (lifetime) of the mentioned Raman modes of  $\text{Bi}_2\text{Te}_3$  in the heterostructure ( $T^* \sim 60$  K) indicates spin-phonon coupling which is, otherwise, not present in an isolated flake.  $\text{Bi}_2\text{Te}_3$  recover its anharmonicity in heterostructure when hexagonal boron nitride (hBN) is placed in between  $\text{Bi}_2\text{Te}_3$

and FePS<sub>3</sub>. Also, the characteristic antiferromagnetic Néel temperature ( $T_N$ ) of FePS<sub>3</sub> reduces from 120 K (in isolated flake) to 65 K, in the heterostructure possibly due to the interfacial strain which leads to smaller Fe-S-Fe bond angles without varying magnetic anisotropic energy (MAE) which has been investigated using density functional theory (DFT) calculations. Spatial control of magnetic proximity-induced spin-phonon coupling in layered stacking of magnetic topological insulator may open up novel pathways for future gate-tunable all-2D spintronic logic devices.

## EXPERIMENTAL DETAILS

Binary Bi<sub>2</sub>Te<sub>3</sub> single crystal was grown through the solid-state reaction method by using box furnace (see the method section for growth details) [30]. Single crystal FePS<sub>3</sub> was grown by the chemical vapor transport (CVT) method in two zone tube furnace as reported in [31]. Bi<sub>2</sub>Te<sub>3</sub> crystal was micromechanically exfoliated by standard scotch tape and transferred onto 300 nm Si/SiO<sub>2</sub> substrate by dry transfer method [32]. Suitable flake was located by using Optical Microscope (OLYMPUS BX53M) by comparing transparency of the flake. Heterostructures consist of Bi<sub>2</sub>Te<sub>3</sub>, FePS<sub>3</sub> and hBN are fabricated by placing one material onto another by using micromanipulator. The fabricated heterostructures (HS) are: (a) HS-1: Bulk Bi<sub>2</sub>Te<sub>3</sub> (>500 nm)/ Bulk FePS<sub>3</sub>(~150 nm); (b) HS-2: Bulk Bi<sub>2</sub>Te<sub>3</sub> (~ 250 nm)/Bulk FePS<sub>3</sub>(~ 88 nm); (c) HS-3: Bulk Bi<sub>2</sub>Te<sub>3</sub> (~140 nm)/ few layer FePS<sub>3</sub>(~10 nm) and (d) HS-4: Bulk Bi<sub>2</sub>Te<sub>3</sub> (>500 nm) /Bulk hBN(>100 nm)/Bulk FePS<sub>3</sub> (~ 150 nm) and (e) HS-5: Bulk Bi<sub>2</sub>Te<sub>3</sub> (>500 nm) /few layer hBN(~10 nm)/Bulk FePS<sub>3</sub> (~ 150 nm) . Room temperature and temperature-dependent Raman measurements of isolated Bi<sub>2</sub>Te<sub>3</sub>, and these heterostructures were carried out by using Jobin Yvon Horibra LABRAM-HR 800 visible micro Raman system and a 473 nm wavelength radiation from a diode laser as an excitation source. All measurements were performed under high vacuum ( $10^{-6}$  mbar) using a liquid helium cryostat (Janis ST-500). Laser beam was focused through a microscope objective with 50x magnification and a spot size of 1 $\mu$ m. Laser power was kept below 200 $\mu$ W to avoid sample heating.

## RESULTS

The crystal structure of Bi<sub>2</sub>Te<sub>3</sub> contains covalently bonded five mono-atomic planes, which form a quintuple layer (Te-Bi-Te-Bi-Te), weakly bound by van der Waals forces. The dynamical

stability of the structure has been confirmed by the absence of imaginary frequencies in the phonon dispersion (see Figure S1). Among 15 zone center phonon branches (12 optical and 3 acoustic) of  $\text{Bi}_2\text{Te}_3$ , 6 of them are Raman active and 6 are infrared (IR) active modes. The irreducible representation for the zone center phonons can be written as  $\Gamma = 2E_g + 2A_{1g} + 2E_u + 2A_{1u}$ , consistent with the point group symmetry  $D_{3d}$  [28]. Here, in-plane  $E_g$  and out-of-plane  $A_{1g}$  modes are Raman active, whereas  $E_u$  and  $A_{1u}$  are IR active mode [33]. The phonon dispersion and calculated Raman active modes of the monolayer  $\text{Bi}_2\text{Te}_3$  (see Figure S1b) agree well with observed Raman shifts at  $106.19 \text{ cm}^{-1}$  ( $E_g$ ) and  $138.26 \text{ cm}^{-1}$  ( $A_{1g}$ ) from polarization-dependent Raman scattering (see Figure 1(b)).

The irreducible representation of the vibrational modes of the  $\text{FePS}_3$  monolayer can be written as  $\Gamma = 8A_g + 6A_u + 7B_g + 9B_u$  consistent with the  $C_{2h}$  point group symmetry of the experimental structure. Among 30 vibrational modes, the  $A_g$  and  $B_g$  modes are Raman-active [34], three modes are acoustic, and the remaining ones are IR-active. The appearance of negative frequencies (imaginary modes) (see Figure S2a) on the phonon dispersion of the  $\text{FePS}_3$  monolayer is likely due to the symmetry along the ferromagnetically coupled zigzag chains of Fe atoms [35]. Introducing symmetry-breaking in that direction leads to a strong structural distortion as two Fe-Fe bond lengths along the zigzag chains are no longer equal (2.78 and 3.73 Å, respectively). This is in contrast to the experimentally determined crystal structures, where ferromagnetically coupled zig-zag chains have a single Fe-Fe bond length of 3.32 Å. Besides, the point group symmetry of this distorted structure is reduced to  $C_s$ , and the lack of centering in the structure doubled the number of vibrational modes of the  $\text{FePS}_3$  monolayer. The phonon dispersion of this low-symmetry distorted structure is shown in Figure S2 (b), and as expected, the imaginary modes no longer exist. The higher wavenumber modes ( $\geq 250 \text{ cm}^{-1}$ ), depicted in Figure 1(c) as SP1 ( $250 \text{ cm}^{-1}$ ), SP2 ( $280 \text{ cm}^{-1}$ ), and SP3 ( $380 \text{ cm}^{-1}$ ), are mostly attributed to the molecular-like vibrations from  $(\text{P}_2\text{S}_6)^{4-}$  bipyramid structures, whereas the low-frequency peaks, zone folded phonons ( $\leq 110 \text{ cm}^{-1}$ ) and magnons ( $\sim 120 \text{ cm}^{-1}$ ), are from vibrations including Fe atoms [26, 29].

Next, we investigated temperature-dependent Raman scattering down to 5 K on HS-1, (see figure 1(a) for reference locations). In case of the heterostructure (HS-1), variation of the classified peaks at low temperature ( $T = 5 \text{ K}$ ) from the room temperature data in terms of peak position, full-width-half-maxima (FWHM), and the intensity can be read by the naked eye and may reveal contributions of phonon anharmonicity and spin-phonon coupling (see Figure 1(b)).

At the heterostructure region, there may be a significant coupling between the adjacent peaks,

as in between broad peak of FePS<sub>3</sub> (denoted as zone folded phonon (ZP) mode around 108 cm<sup>-1</sup>) and characteristic E<sub>g</sub><sup>2</sup> mode (designated as E1 in Figure 1(b)) of Bi<sub>2</sub>Te<sub>3</sub>, which are characteristic phonon modes of individual compounds. Deconvolution of the hybrid peak around 110 cm<sup>-1</sup> into two Lorentzian curves confirms that the broad ZP peak of FePS<sub>3</sub> becomes sharply peaked (100 times at 5 K) in presence of the underneath Bi<sub>2</sub>Te<sub>3</sub> layer. Note that the disappearance of the broad peak around 100 cm<sup>-1</sup> in the overlapping region at low temperature (~ 100 K) is remindful of the pristine FePS<sub>3</sub>, as reported in [26]. To investigate the temperature dependent phonon behavior, the frequency ( $\omega$ ) and the linewidth ( $\Gamma$ ) are extracted from the respective Lorentzian fits to specific phonon modes and were fit by symmetric three phonon coupling model (see Figure 2-3) [36]:

$$\omega(T) = \omega_1 + \frac{\omega' - \omega_1}{1 + \exp[\frac{T-T_0}{dT}]} \quad (1)$$

$$\Gamma = \Gamma_0 \left( 1 + \frac{1}{\exp(\frac{hc\bar{\nu}_1}{k_B T}) - 1} + \frac{1}{\exp(\frac{hc\bar{\nu}_2}{k_B T}) - 1} \right) \quad (2)$$

Here, the parameters  $\omega'$  and  $\omega_1$  represent the top and bottom of the fitted sigmoidal curve, respectively;  $T_0$  is the center point, and  $dT$  controls the width of the curve.  $h$  and  $k_B$  are the Planck and Boltzmann constants, respectively,  $c$  is the speed of light and  $T$  is the temperature.  $\Gamma_0$  is the asymptotic value of the linewidth at zero temperature.  $\bar{\nu}_1$  and  $\bar{\nu}_2$  are two acoustic phonon modes with different wavenumbers with opposite wavevector.

In the isolated Bi<sub>2</sub>Te<sub>3</sub> (see the inset of Figure 3(a)), no phonon anomaly was observed in the peak position and linewidth of the phonon modes, possibly due to the dominant phonon-phonon scattering [27]. The observed anharmonic behaviour is independent of the excitation wavelength [27], different structural form (bulk single crystal [37], nanowires, nanoribbons [38] etc.), and the thickness [27, 39] of Bi<sub>2</sub>Te<sub>3</sub> (see Supplemental Table VIII). The behavior can simply be described by the above mentioned symmetric three-phonon coupling model [40] where a zone centre optical phonon decays into two acoustic phonons with equal energies and opposite momenta. Note that the fitting of the temperature dependent peak positions of the in-plane and out-of- plane phonon modes of isolated Bi<sub>2</sub>Te<sub>3</sub> (see inset of Figure 3(a),(c)) and FePS<sub>3</sub> connected to the heterostructure (HS-1) is depicted in the Supplementary Information (Figure S3) [41].

In case of FePS<sub>3</sub>, in the heterostructure (HS-1), at/around 65 K, SP1-SP3 modes show deviation from the anharmonic fit for each of the phonon frequencies [see Figure 2(a),(c),(e)]. Note that antiferromagnetic ordering sets in ( $T_N$ ) at 120 K, irrespective of the thickness of the FePS<sub>3</sub>

flake [26]. Also, no such changes were detected for the linewidth, may be due to the insignificant contribution of spin-phonon interaction to the phonon relaxation process [42]. The nature of the temperature dependent linewidth also suggests that the effect of phonon-impurity scattering, and electron-phonon interaction can be ruled out, as discussed in [28], whereas the violation of three phonon anharmonic decay model was observed in the linewidth of FePS<sub>3</sub> spin-phonon coupled modes (see figure 2(b),(d)) in the heterostructure due to Bi<sub>2</sub>Te<sub>3</sub> underneath.

Noticeably, in the Bi<sub>2</sub>Te<sub>3</sub>/FePS<sub>3</sub> heterostructure (HS-1), the enhancement of the intensity in all the Raman modes of FePS<sub>3</sub>, compared to the isolated flake, can be explained by the electron transfer at the Bi<sub>2</sub>Te<sub>3</sub>/FePS<sub>3</sub> interface. Adopting a simple model where the interface has been treated as a metal (Bi<sub>2</sub>Te<sub>3</sub> is sufficiently n doped with  $n \sim 10^{19} \text{ cm}^{-3}$ ) [43] - semiconductor (FePS<sub>3</sub> with bandgap 1.60 eV) junction, band alignment, depicted in Figure S4, indicates that the electrons will be transferred from FePS<sub>3</sub> into the Bi<sub>2</sub>Te<sub>3</sub>. The barrier ( $E_{bar} \sim 1.17 \text{ eV}$ ) formed at the interface, which is the difference between the work functions of the Bi<sub>2</sub>Te<sub>3</sub> ( $\phi_{BT} \sim 5.30 \text{ eV}$ ) [44] and the FePS<sub>3</sub> ( $\phi_{FPS} \sim 4.13 \text{ eV}$ ), is less than the excitation wavelength (2.62 eV). Consequently, available transitions for the Raman scattering may involve real energy levels which drastically enhances the intensity of the characteristic Raman modes of FePS<sub>3</sub> [45].

One-magnon mode ( $M$ ) at  $120 \text{ cm}^{-1}$  at a temperature ( $T_M \sim 60 \text{ K}$ ) was observed in FePS<sub>3</sub>. Softening of this magnon mode appears at 30 K with  $\Delta\omega \sim 4 \text{ cm}^{-1}$  in FePS<sub>3</sub> connected to heterostructure (HS-1) (see figure S5(a)) while, this anomaly occurs at 15 K [Fig.2(f)] with very small  $\Delta\omega \sim 0.56 \text{ cm}^{-1}$  due to Bi<sub>2</sub>Te<sub>3</sub> underneath, in the heterostructure [26, 29]. Additionally, magnetic field dependent Raman scattering at 4 K offers an insightful observation on the splitting of the magnon mode in the heterostructures. By applying a magnetic field perpendicular to the  $ab$  plane of the HS-1, magnon-gap excitation can be splitted into two components (linear in B with  $g$ -factor close to 2.15) following the easy-axis antiferromagnetic properties which has already been reported by Vaclavkova *et al.* for the isolated FePS<sub>3</sub> [29]. Moreover, no such changes in the strength of magnon-phonon coupling ( $\sim 3 \text{ cm}^{-1}$ ) was observed in the case of heterostructure. In due course, while applying magnetic field parallel to the  $ab$  plane of the HS-1, magnon mode of FePS<sub>3</sub> splits at much lower magnetic field ( $\sim 9 \text{ T}$ ) compared to in-plane splitting field in isolated FePS<sub>3</sub> ( $\sim 16 \text{ T}$ ) reported in [29]. Note that the Raman modes of isolated Bi<sub>2</sub>Te<sub>3</sub> shows no magnetic field dependence in either configuration, as also reported in previous studies [27] (see Supplemen-



tary Information Figure S24, Table IX) . To understand the reduction of the external “in-plane” magnetic field required for the splitting of the magnon in the HS-1, one can speculate the effect of the time-independent antidamping torque which may generate further “in-plane” field-like effect predicted for antiferromagnetic topological insulators with preserving the gapless states in TI [46] (see Supplementary Information Figure S24 , Table IX). Besides, to inspect the origin of the possible magnon temperature reduction in hybrid FePS<sub>3</sub>, the spin wave stiffness constant ( $D$ ) which is linked to the long wavelength limit of the acoustic mode of magnon dispersion can be determined. Our noncollinear density functional theory (ncDFT) calculations (see the methodology for computational details) predict that monolayer FePS<sub>3</sub> has spin wave stiffness of 245 meVÅ<sup>2</sup>. Interestingly,  $D$  value gets reduced to 158 meVÅ<sup>2</sup> for FePS<sub>3</sub> deposited onto six quintuple layer (6QL) of Bi<sub>2</sub>Te<sub>3</sub>.

Figure 3 presents the temperature dependence of the in-plane and the out-of-plane phonon modes of Bi<sub>2</sub>Te<sub>3</sub> in the heterostructure. Unlike pristine Bi<sub>2</sub>Te<sub>3</sub> (see the inset of Figure 3a and 3c) [27], at/around 60 K, respective phonon modes,  $E_g^2$  (see Figure 3a) and  $A_{1g}^2$  (see Figure 3c), show clear deviation ( $\Delta\omega_{5K}$ ) of 1.56 cm<sup>-1</sup> and 1.62 cm<sup>-1</sup> from the anharmonic fit, respectively. Regarding linewidth, while  $E_g^2$  mode shows slight deviation ( $\sim 0.56$  cm<sup>-1</sup>) in the phonon behaviour around 60 K (see Figure 3b), no such abrupt changes were observed for  $A_{1g}^2$  mode (see Figure 3d). Theoretically, spin-phonon coupling can be introduced as spin susceptibility ( $\chi_M$ ) in the phonon self energy (SE) which consists of the real (frequency shift) and the imaginary part (line broadening) ( $\Delta(\omega_j(q), T) + i\Gamma(\omega_j(q), T)$ ), analogous to modification due to electron-phonon coupling [27]. On account of this, from our result, a clear departure of  $\chi_M$  from the usual phonon behavior in the Bi<sub>2</sub>Te<sub>3</sub> can be identified at/around 60 K in the heterostructure (see Figure S6(a), (b)). Thickness dependent Raman measurements were done on Bi<sub>2</sub>Te<sub>3</sub>/FePS<sub>3</sub> heterostructures (HS-2, HS-3) with temperature ranging from 5 K to 300 K. The coupling strength was observed to be high for the heterostructure consisting of thick-layer Bi<sub>2</sub>Te<sub>3</sub> and FePS<sub>3</sub>. Strength of spin-phonon coupling of Raman modes of Bi<sub>2</sub>Te<sub>3</sub> decreases with the reduction of thickness (see fig. S8) of individual material as observed in [47]. In the heterostructure, with reduced thickness, surface phonon polariton is red shifted and as a result, it becomes off-resonant with antiferromagnetic magnon, which, in-turn, reduces the coupling strength of the hybridized quasi-particle. The deviation from the phonon anharmonicity  $\Delta\omega$  (related to square of magnetization) decreases with lowering the thickness of Bi<sub>2</sub>Te<sub>3</sub> and FePS<sub>3</sub> in heterostructures. In the case of HS-1, the value of  $\Delta\omega$  is close to 1.21 which is higher than the recorded values for HS-2 ( $\Delta\omega \sim 0.69$ ) and HS-3 ( $\Delta\omega \sim 0.57$ ) for the in-plane and out-of-plane Raman modes of Bi<sub>2</sub>Te<sub>3</sub>. The deviation ( $\Delta\omega$ ) is more prominent

in out-of-plane mode ( $A_{1g}^2$ ) of  $\text{Bi}_2\text{Te}_3$  in case of few layer heterostructure (see fig. S8(d)) since Bi and Te atoms vibrate perpendicularly to the layer surface for  $A_{1g}^2$  mode [48]. The coupling strength decreases but the characteristic temperature for spin-phonon coupling of  $\text{Bi}_2\text{Te}_3$  remains invariant ( $\sim 60$  K) with reduction of thickness (see fig. S8). The robustness of spin-phonon coupling of  $\text{Bi}_2\text{Te}_3$  in  $\text{Bi}_2\text{Te}_3/\text{FePS}_3$  heterostructure (HS-4, HS-5) could be destroyed by inserting hexagonal boron nitride (hBN) in between  $\text{Bi}_2\text{Te}_3$  and  $\text{FePS}_3$  (see Figure 5). The insulating nature of the  $\text{FePS}_3$  with highly transparent hBN [49] in the middle of the stacked assembly make the laser penetration depth very large (also recognizable under optical microscope), which in turn facilitates the recording of the characteristic Raman modes of individual materials even in bulk thicknesses (see Figure 5(b)). No such phonon anomaly (independent of the thickness of hBN) was observed in the in-plane and out-of-plane Raman modes of  $\text{Bi}_2\text{Te}_3$  (see Figure 5(c), (d)), similar to the case of isolated  $\text{Bi}_2\text{Te}_3$ .

Typical example of magnetic proximity effect [50–53] is the extension of the spin order beyond the interface of diluted magnetic semiconductors (DMS), namely (Ga, Mn)As, and Fe overlayer through an anti-parallel alignment. Avoiding the effect of diffusion/segregation in DMS subsystem, nontrivial surface state of TI in contact with FMI can be understood from the propagation of spin-polarized charge carriers resulting in building up finite spin polarization close to the interface [54]. Moreover, presence of the TI’s conducting surface states is crucial for the spin polarized charge transfer [53, 55]. On a related note, diffusion of the magnetic atoms (*e.g.* Eu atoms in EuS) into the first QL of TI (*e.g.*  $\text{Bi}_2\text{Se}_3$ ) during the growth of the heterostructure can be the origin of “interface ferromagnetism”, as reported in [56]. But, in the concerned study, heterostructure has been formed *via* stamping of one vdW material onto another, eliminating the possibility of diffusion which usually happens during the thin film growth [57]. Interfacial ferromagnetism remains evident up to room temperature in  $\text{Bi}_2\text{Se}_3/\text{EuS}$  heterostructure. Significant enhancement of  $T_C$  was observed at the interface arising from large spin–orbit interaction and spin–momentum locking of the topological insulator surface [58]. In  $\text{Bi}_2\text{Te}_3/\text{Fe}_3\text{GeTe}_2$  heterostructure,  $T_C$  enhances up to 400 K, which is attributed to the interfacial exchange coupling effect between  $\text{Bi}_2\text{Te}_3$  and  $\text{Fe}_3\text{GeTe}_2$ , which induces the enhancement of  $T_C$  for the 2D ferromagnetism [59]. The enhancement of  $T_C$  of  $\text{Cr}_2\text{Ge}_2\text{Te}_6$  from 65 K to 150 K was observed in  $\text{W}/\text{Cr}_2\text{Ge}_2\text{Te}_6$  heterostructure due to the formation of W-Te bonding at the interface [60]. In the stacked structure, strain engineering may enhance the  $T_C$  by raising the exchange energy between the cation sites which may be mediated by the polarized anion atoms [59]. But even for the fully epitaxial vdW heterostructure (*e.g.*  $\text{Fe}_x\text{Cu}_{1-x}\text{Se}$

and  $\text{Bi}_2\text{Te}_3$ ), lattice mismatch, as large as 20%, may occur through van der Waals bonding across the interface [61]. For a typical sample size of sub-micrometer length scale, structural, chemical and electronic analysis of the heterointerface as formed in the vdW stacking, can be probed by low-energy electron microscopy (LEEM), which is beyond the scope of the current work [62, 63]. However, in our micromanipulated vdW  $\text{Bi}_2\text{Te}_3/\text{FePS}_3$  heterostructure, possible strain has been calculated as low as 0.5%.

The magnetic and electronic properties of the  $\text{Bi}_2\text{Te}_3/\text{FePS}_3$  heterostructure have been investigated by performing DFT calculations using a supercell containing both individual layers coupled weakly by the vdW interaction (see methods for details). Since the point group symmetry ( $D_{3d}$ ) remains invariant with the thickness of  $\text{Bi}_2\text{Te}_3$ , we have considered  $\text{Bi}_2\text{Te}_3$  monolayer for our calculations to save computational time. Note that no significant Raman shift was observed in the in-plane phonon characteristic mode ( $E_g^2$ ) of  $\text{Bi}_2\text{Te}_3$ , whereas, out-of-plane Raman mode ( $A_{1g}^2$ ) shows a maximum shift of  $6 \text{ cm}^{-1}$  with thickness [48, 64, 65] (See Supplementary Information Table IV, Table VII). In the context of the current study, temperature dependent phonon anomaly as detected from the deviation from anharmonicity, in phonon frequency for a certain thickness is conceptually different from the thickness dependent variation of Raman shift. Contrastingly, all phonon modes of  $\text{FePS}_3$  hardly show any Raman shift with decreasing thickness down to monolayer (see Supplementary Information, Figure S23, Table VI). It is worth mentioning that  $\text{FePS}_3$  exhibits layer thickness independent transition temperature ( $T_N \sim 120 \text{ K}$ ) from bulk to monolayer [66]. In this framework, the S-termination of the  $\text{FePS}_3$  layer (on top of the  $\text{Bi}_2\text{Te}_3$  layer) is energetically the most stable configuration, and the stoichiometry of each individual layer is also maintained. Interestingly, the magnetic ground state (z-AFM order; cf. (Fig. 4a) of the  $\text{FePS}_3$  layer remains unchanged even in this heterostructure set-up. The robustness in AFM order of  $\text{FePS}_3$  compound [66] from bulk to monolayer to heterostructure is promising for device applications. We obtain  $\sim 3.5 \mu_B$  magnetic moment at the  $\text{Fe}^{2+}$  sites, whereas the other atoms have negligibly small moments ( $< 0.1 \mu_B$ ). Furthermore, the nature of the spin anisotropy of the interface  $\text{FePS}_3$  layer was determined from our calculated magnetocrystalline anisotropy energies (MAE). The obtained MAE ( $E_{in-plane} - E_z$ ) value  $1.31 \text{ meV/f.u.}$  of the  $\text{FePS}_3$  layer indicates the easy axis (out-of-plane) of magnetic anisotropy of the system. Relatively large MAE value [67] originates from the strong spin-orbit coupling (SOC) in the  $\text{Bi}_2\text{Te}_3/\text{FePS}_3$  heterostructure. In contrast, magnetic shape anisotropy (MSA), which represents the anisotropic dipolar interaction of free magnetic poles and tends to align magnetic moments parallel to surfaces, only plays a sig-

nificant role when SOC is weak [67]. MSA values are generally in the order of  $\mu\text{eV}$ , and thus, they are negligible for  $\text{Bi}_2\text{Te}_3/\text{FePS}_3$  heterostructure. Therefore, the long-range order observed in the  $\text{Bi}_2\text{Te}_3/\text{FePS}_3$  heterostructure is primarily governed by MAE. The GGA+ $U$ +SOC electronic structures (Fig 4b) of the  $\text{Bi}_2\text{Te}_3/\text{FePS}_3$  heterostructure reveal that the system is a narrow band-gap (0.25 eV) semiconductor. The atom-projected density of states (DOS) shows that the bands below the Fermi level (FL) are predominantly occupied by Bi and Te valence states, and there is a strong hybridization between the Fe  $d$  levels and the valence-band orbitals of  $\text{Bi}_2\text{Te}_3$ . Since this hybridization is spin-dependent, the proximity exchange could be significant [68] and may lead to gaped surface states as opposed to the metallic surface states of isolated  $\text{Bi}_2\text{Te}_3$  (see Figure S5(b)). Note that scanning tunnelling spectroscopy on  $\text{Bi}_2\text{Te}_3/\text{FePS}_3$  heterostructure may invoke insights into the atomistic origin of the proximitized magnetic ordering which is beyond the scope of the current work.

To understand the microscopic origin of the reduction of  $T_N$  of  $\text{FePS}_3$  in the heterostructure, we calculate the interface AFM exchange ( $J_{int}$ ) by using the energy difference between FM and z-AFM spin configurations after mapping them to the Heisenberg model  $H = J_{int} \sum_{i>j} S_i \cdot S_j$  (cf. supplemental materials S7 for details). We estimate  $J_{int}$  to be 69 K, lower than the AFM exchange  $J_{ML}$  of the  $\text{FePS}_3$  monolayer (110 K). The lowering of AFM exchange in the  $\text{Bi}_2\text{Te}_3/\text{FePS}_3$  heterostructure is consistent with the experimentally observed trend in  $T_N$ . In  $\text{FePS}_3$ , Fe atoms are in an edge-sharing octahedral environment with their neighboring S, and in this case, the Fe-S-Fe bond angle is close to  $90^\circ$ . In this situation, direct d-d hopping, which gives rise to an antiferromagnetic exchange competes with the FM superexchange [69, 70]. In the 0.5% bi-axial strained structure of the  $\text{FePS}_3$  monolayer, the Fe-S-Fe bond angle is  $\sim 10^\circ$  smaller than the unstrained structure, whereas the Fe-Fe bond length remains almost the same. Due to this reason, the effective AFM interaction ( $J_{ML} = 80$  K) of the strained  $\text{FePS}_3$  monolayer gets weakened by the enhancement of FM superexchange. In  $\text{Bi}_2\text{Te}_3/\text{FePS}_3$  monolayer, we also observe a similar trend with higher reduction in Fe-S-Fe bond angles, and thus the overall AFM exchange becomes much weaker. Therefore, the interfacial strain which leads to smaller Fe-S-Fe bond angles could primarily attribute to the lowering of  $J_{int}$  in the heterostructure system. The nature of the strain demonstrated in the calculations corresponds to compressive biaxial strain for the  $\text{FePS}_3$  monolayer. Similar strain effects due to the lattice mismatch at the vdW interface between  $\text{Bi}_2\text{Te}_3$  and  $\text{FePS}_3$  was observed (See Supplementary Information Table V). In case of  $\text{FePS}_3$  connected to the

heterostructure, reduction of  $T_N$  was observed at/around 65 K (see supplementary information Fig. S3). The interfacial strain arises due to the lattice mismatch, which propagates laterally through the layer at a certain distance ( $\sim 100$  nm) from the edge of the interface and decreases with the distance as reported in previous computational studies [71]. Similar hetero-bonding effect due to strain has been detected in  $\text{WSe}_2\text{-MoS}_2$  heterostructure *via* scanning probe microscopy [72]. In our case, the strain propagation is the most probable origin of the reduced  $T_N$  in  $\text{FePS}_3$  connected to the heterostructure (beyond overlapping region), as depicted in the supplemental figure (Fig. S3). A proper mapping of the two-dimensional strain tensor (in-plane) would be necessary to understand the precise extension of the decay. Further studies, like spin-polarized scanning probe microscopy, are required for an atomistic picture of strain distribution. In the current work, in spite of the reduction in  $T_N$ , increment of the sublattice magnetization of  $\text{FePS}_3$  in case of the heterostructure can be observed as  $\Delta\omega$  value is enhanced by 4 times compared to isolated  $\text{FePS}_3$  which may result in better device performance, may be realized *via* magneto-transport measurement.

A sharp decrease in the Raman shift is observed at 30 K (see figure 3(a),(c)) in both modes of  $\text{Bi}_2\text{Te}_3$  in the heterostructure. This could be understood from the temperature-dependent antiferromagnetic order parameter. The magnetization of the bulk state falls faster than the surface states with temperature (see figure S9 (a),(b)) as reported in [73]. In mean field approximation, one can relate  $\Delta\omega$  to magnetization as  $\Delta\omega(T) \propto \frac{M^2(T)}{M_{max}^2}$ . Magnetization ( $M$ ) is plotted with temperature for the phonon modes of  $\text{Bi}_2\text{Te}_3$  in the heterostructure (see figure S9 (a),(b)) and fit with  $M \approx |(1 - \frac{T}{T_N})|^\beta$  equation, where  $\beta$  is the critical exponent.  $\beta$  value at 60 K (0.15) corroborates with 2D Ising model, the origin of the surface magnetic contribution comes from  $\text{FePS}_3$  and the  $\beta$  value at 30 K (0.35) corresponds to 3D Heisenberg model, responsible for bulk contribution. The exponent value,  $\beta$  for isolated  $\text{FePS}_3$  and  $\text{FePS}_3$  in the heterostructure are close to the mean field (see figure S9(c)). With decreasing the  $\text{Bi}_2\text{Te}_3$  layers, proximity induced bulk magnetization (related to  $\Delta\omega$ ) in  $\text{Bi}_2\text{Te}_3$  decreases and as a result coupling strength at the interface was also reduced. Induced bulk magnetization reduces more than 4 times in  $\text{Bi}_2\text{Te}_3$  when thickness of  $\text{Bi}_2\text{Te}_3$  reduces from  $\sim 500$  nm (HS-1) to  $\sim 12$  nm (HS-II) (see supplementary figure, Fig. S25).

Now we turn to discuss the spin-phonon coupling of the  $\text{Bi}_2\text{Te}_3/\text{FePS}_3$  heterostructure. This complex heterostructure has a  $P_1$  space group and  $C_1$  point group symmetry, and due to having a large number of atoms in the supercell, the phonon calculation of this heterostructure is very expensive. Therefore, we calculate the phonons of individual monolayers and combine them together

to understand the Raman data of the  $\text{Bi}_2\text{Te}_3/\text{FePS}_3$  heterostructure. The spin-phonon coupling parameter of the  $\text{FePS}_3$  monolayer has been estimated from the shift in  $\Gamma$ -phonons due to a change in magnetic order from z-AFM to FM. The Raman active modes corresponding to both magnetic order and relative change in phonon frequencies ( $\Delta_\lambda^{rel} = \frac{\omega_{FM} - \omega_{z-AFM}}{\omega_{z-AFM}}$ ) are listed in Supplemental Table 2. The significant change in phonon frequencies due to a change in magnetic order indicates the strong coupling between magnetic and lattice degrees of freedom in the  $\text{FePS}_3$  monolayer.

In particular,  $115 \text{ cm}^{-1}$  and  $141 \text{ cm}^{-1}$   $A_g$  modes of  $\text{FePS}_3$  show significant spin-phonon couplings. Interestingly, the frequencies of these two modes are close to the phonon frequency of  $E_g$  and  $A_{1g}$  modes of  $\text{Bi}_2\text{Te}_3$  (Supplemental Table 1). There is a possibility that the  $\text{Bi}_2\text{Te}_3$  modes would couple to phonons of similar frequencies of  $\text{FePS}_3$  due to resonance, and the hybrid modes appear in the Raman spectrum. Such coupling phenomena were reported in earlier literature [74], where magnon excitations with Raman-allowed symmetries couple to similar frequency phonon modes showing strong spin-phonon coupling. In order to illustrate the temperature dependence of the hybrid modes, we consider the Ginzburg-Landau (GL) theory formalism [74]. Due to the spin-phonon coupling, the phonon frequency will vary with temperature below  $T_N$  as the z-AFM order sets in, and the modified phonon frequency is given by the formula:

$$\omega_\lambda = 2 \Delta_\lambda m^2 + \sqrt{\omega_{0\lambda}^2 + 4 \Delta_\lambda^2 m^4} \quad (3)$$

where  $m \sim (1 - \frac{T}{T_N})^\beta$  is the magnetic order parameter,  $\omega_{0\lambda}$  is the high-temperature ( $T \geq T_N$ ) phonon frequency the  $\lambda_{th}$  phonon mode, and  $\Delta_\lambda$  is the spin-phonon coupling parameter derived from the DFT calculations. The temperature dependence of the coupled hybrid modes is shown in Fig 4(c-d). One can see both phonon frequencies increase with increasing temperature which qualitatively agrees with the trend observed in experiments. The spin-phonon coupled hybrid modes in the heterostructure could be attributed to the phonon-resonance phenomenon due to the proximity effect.

## CONCLUSION

In conclusion, we report a proximate AFM order in  $\text{Bi}_2\text{Te}_3$ , a topological insulator, by investigating the temperature-dependent Raman spectroscopy of  $\text{Bi}_2\text{Te}_3$  (TI)-  $\text{FePS}_3$  (AFM with  $T_N \sim 120 \text{ K}$ ) stacked vdW heterostructure down to 5 K. Unlike isolated  $\text{Bi}_2\text{Te}_3$ , a deviation from the usual phonon anharmonicity in Raman modes corresponding to  $\text{Bi}_2\text{Te}_3$  in the heterostructure was

observed at 60 K and can be correlated to antiferromagnetic proximity induced spin-phonon coupling. The strength of spin-phonon coupling decreases with the reduction of thickness of  $\text{Bi}_2\text{Te}_3$  and  $\text{FePS}_3$  in heterostructure, but the characteristic temperature for spin-phonon coupling remains invariant ( $\sim 60$  K). The robust spin-phonon coupling in  $\text{Bi}_2\text{Te}_3$  could be destroyed by placing hBN in between  $\text{Bi}_2\text{Te}_3$  and  $\text{FePS}_3$  in the heterostructure. Also, a reduction of  $T_N$  to 65 K of hybrid  $\text{FePS}_3$  was identified, possibly due to the interfacial strain which leads to smaller Fe-S-Fe bond angles as corroborated by DFT calculations. The current study on the spatial variation of spin-phonon coupling at the interface of vdW magnet-TI heterostructure may be crucial for the future spin logic devices.

## Methods

### Sample preparation

Binary  $\text{Bi}_2\text{Te}_3$  single crystal was grown through solid-state reaction method by using box furnace. Bismuth powder (Alfa Aesar, purity 99.999% ), Tellurium powder (Alfa Aesar , purity 99.999% ) were mixed in proper stoichiometric ratio and sealed into a quartz ampoule under vacuum ( $\approx 10^{-5}$  mbar). The ampoule was then placed at the centre of the furnace and heated at  $700^\circ\text{C}$  for seven days [30].

### Computational Details

Density functional theory (DFT) calculations have been performed by using a plane-wave basis set with a kinetic energy cutoff of 400 eV and projector augmented-wave [75, 76] potentials as implemented in the Vienna Ab initio Simulation Package (VASP) [77, 78]. For the exchange-correlation functional, the Perdew-Burke-Ernzerhof (PBE) [79] version of the generalized gradient approximation (GGA) has been used. In our calculations, the spin-polarized case for  $\text{FePS}_3$  and the non-spin-polarized case for  $\text{Bi}_2\text{Te}_3$  have been considered. During structural relaxations, the positions of the ions were relaxed until the Hellman-Feynman forces became less than  $0.001\text{ eV/\AA}$ . Correlation effects for Fe  $d$  electrons have been incorporated within GGA+ $U$  [80] approach, and an effective on-site Coulomb repulsion  $U_{eff} = 3\text{ eV}$ , which is within the range of  $U$  values used for [81–83] has been considered. In addition, spin-orbit coupling (SOC) was included in our calculations to get the correct electronic band dispersion for  $\text{Bi}_2\text{Te}_3$  and estimate the magnetic anisotropy for  $\text{FePS}_3$ . Phonons were calculated using the density functional perturbation theory (DFPT) [84] as implemented in the PHONOPY [85].

The  $\text{Bi}_2\text{Te}_3$ - $\text{FePS}_3$  heterostructure has been constructed within the Quantum ATK framework [86]. The surface matching algorithm described in ref [87] was utilized to obtain low-strain

hetero-interfaces. For this heterostructure, the mean absolute strain values on both the monolayer surfaces were calculated as  $\sim 0.5\%$ . The composite supercell was then fully relaxed within the vdW correction method DFT-D3 [88] until forces on atoms became less than  $0.02 \text{ eV/\AA}$ . The reciprocal space integration was carried out with a  $\Gamma$  centered k-mesh of  $8 \times 8 \times 2$  for  $\text{Bi}_2\text{Te}_3$  bulk,  $12 \times 12 \times 1$  for  $\text{Bi}_2\text{Te}_3$  single layer,  $12 \times 8 \times 1$  for  $\text{FePS}_3$  monolayer, and  $2 \times 2 \times 1$  for the  $\text{Bi}_2\text{Te}_3$ - $\text{FePS}_3$  heterostructure.

For Magnon Stiffness Calculation, We employ the interface builder in the QuantumATK package [86] to construct a unit cell of the 1ML- $\text{FePS}_3$ /6QL- $\text{Bi}_2\text{Te}_3$  heterostructure with  $2 \times 2$  supercell of  $\text{FePS}_3$  and  $\sqrt{7} \times \sqrt{7}$  supercell of  $\text{Bi}_2\text{Te}_3$ . Spin wave stiffness constant  $D$  of 1ML- $\text{FePS}_3$  /6QL- $\text{Bi}_2\text{Te}_3$  heterostructure is calculated using Green's function (GF) formalism of Ref. [89], as implemented in QuantumATK package [86]. The Kohn-Sham Hamiltonian of density functional theory (DFT), as the input of GF formalism, is obtained from noncollinear DFT calculations using the Perdew-Burke-Ernzerhof (PBE) parametrization [90] of the generalized gradient approximation (GGA) to the exchange-correlation functional, as implemented in QuantumATK package [86]; norm-conserving fully relativistic pseudopotentials of the type PseudoDojo-SO [86, 91] for describing electron-core interactions; and the PseudoDojo (medium) numerical linear combination of atomic orbitals (LCAO) basis set [91]. The energy mesh cutoff for the real-space grid is chosen as 101 Hartree, and the k-point grid  $6 \times 6 \times 1$  is used for the self-consistent calculations. Periodic boundary condition is used for the self-consistent calculations, and a  $15\text{\AA}$  vacuum is placed on the top of heterostructure in order to remove interaction between the consecutive periodic image.

### Acknowledgments

The authors would like to thank Dr. Vasant Sathe, Prof. K Sengupta, Dr. Marek Potemski, Dr. Clément Faugeras, Prof. Achintya Singha, Mr. Somsubhra Ghosh, Dr. Mintu Mondal, and Dr. Devajyoti Mukherjee for fruitful discussion. SMAity and TK are grateful to DST-INSPIRE for their fellowships. D.D. and L.Y. gratefully acknowledge the U.S. DOE, Office of Science, Office of Basic Energy Sciences, under Award No. DE-SC0021127 for financial assistance and Advanced Computing Group of the University of Maine System for providing computational resources for this work. SMasanta is grateful to Council of Scientific & Industrial Research (CSIR), New Delhi, for the financial support through the award of NET-SRF (File No: 09/015(0531)/2018-EMR-I). The authors are thankful to the facilities at UGC-DAE-CSR-Indore. Magneto-Raman scattering at low temperature were performed at LNCMI, European Magnetic Field Laboratory at Grenoble under the project GSC08-119. SMAity would like to thank Ms. Diana Vaclavkova, Ms. Anushree



Dey, Mr. Sanjib Naskar, Mr. Rahul Paramanik and Mr. Soumik Das. MP and BD is grateful to IACS for the fellowship. SD acknowledges the financial support from DST-SERB grant No. ECR/2017/002037, SCP/2022/000411 and CRG/2021/004334. SD also acknowledges support from the Central Scientific Service (CSS) and the Technical Research Centre (TRC), IACS, Kolkata.

---

- [1] S. V. Eremeev, V. N. Men'shov, V. V. Tugushev, P. M. Echenique, and E. V. Chulkov, [Phys. Rev. B \*\*88\*\*, 144430 \(2013\)](#).
- [2] M. Liu, J. Zhang, C.-Z. Chang, Z. Zhang, X. Feng, K. Li, K. He, L.-I. Wang, X. Chen, X. Dai, Z. Fang, Q.-K. Xue, X. Ma, and Y. Wang, [Phys. Rev. Lett. \*\*108\*\*, 036805 \(2012\)](#).
- [3] Y. L. Chen, J.-H. Chu, J. G. Analytis, Z. K. Liu, K. Igarashi, H.-H. Kuo, X. L. Qi, S. K. Mo, R. G. Moore, D. H. Lu, M. Hashimoto, T. Sasagawa, S. C. Zhang, I. R. Fisher, Z. Hussain, and Z. X. Shen, [Science \*\*329\*\*, 659 \(2010\)](#), <https://www.science.org/doi/pdf/10.1126/science.1189924>.
- [4] J. Henk, M. Flieger, I. V. Maznichenko, I. Mertig, A. Ernst, S. V. Eremeev, and E. V. Chulkov, [Phys. Rev. Lett. \*\*109\*\*, 076801 \(2012\)](#).
- [5] T. K. Dalui, P. K. Ghose, S. Majumdar, S. K. Mahatha, F. Diekmann, K. Rossnagel, R. Tomar, S. Chakraverty, A. Berlie, and S. Giri, [Phys. Rev. B \*\*103\*\*, 064428 \(2021\)](#).
- [6] Y. Fan, X. Kou, P. Upadhyaya, Q. Shao, L. Pan, M. Lang, X. Che, J. Tang, M. Montazeri, K. Murata, L. Chang, M. Akyol, G. Yu, T. Nie, K. Wong, J. Liu, Y. Wang, Y. Tserkovnyak, and K. Wang, [Nature Nanotechnology \*\*11\*\*, 352 \(2016\)](#).
- [7] I. Lee, C. K. Kim, J. Lee, S. J. L. Billinge, R. Zhong, J. A. Schneeloch, T. Liu, T. Valla, J. M. Tranquada, G. Gu, and J. C. S. Davis, [Proceedings of the National Academy of Sciences \*\*112\*\*, 1316 \(2015\)](#), <https://www.pnas.org/doi/pdf/10.1073/pnas.1424322112>.
- [8] I. Vobornik, U. Manju, J. Fujii, F. Borgatti, P. Torelli, D. Krizmancic, Y. S. Hor, R. J. Cava, and G. Panaccione, [Nano Letters \*\*11\*\*, 4079 \(2011\)](#), PMID: 21861485, <https://doi.org/10.1021/nl201275q>.
- [9] Q. I. Yang, M. Dolev, L. Zhang, J. Zhao, A. D. Fried, E. Schemm, M. Liu, A. Palevski, A. F. Marshall, S. H. Risbud, and A. Kapitulnik, [Phys. Rev. B \*\*88\*\*, 081407 \(2013\)](#).
- [10] M. Blei, J. Lado, Q. Song, D. Dey, O. Erten, V. Pardo, R. Comin, S. Tongay, and A. Botana, [Applied Physics Reviews \*\*8\*\* \(2021\)](#).
- [11] Q. He, X. Kou, A. Grutter, L. Pan, X. Che, Y. Liu, T. Nie, S. Disseler, B. Kirby, I. Ratcliff, Q. Shao,

- K. Murata, Y. Fan, M. Montazeri, J. Borchers, K. Wang, and B. Zhang, *Nature materials* **16** (2016).
- [12] A. K. Geim and I. V. Grigorieva, *Nature* **499**, 419 (2013).
- [13] H. X. Yang, A. Hallal, D. Terrade, X. Waintal, S. Roche, and M. Chshiev, *Phys. Rev. Lett.* **110**, 046603 (2013).
- [14] Z. Qiao, W. Ren, H. Chen, L. Bellaïche, Z. Zhang, A. H. MacDonald, and Q. Niu, *Phys. Rev. Lett.* **112**, 116404 (2014).
- [15] P. Wei, S. Lee, F. Lemaitre, L. Pinel, D. Cutaia, W. Cha, F. Katmis, Y. Zhu, D. Heiman, J. Hone, J. S. Moodera, and C.-T. Chen, *Nature materials* **15**, 711—716 (2016).
- [16] J. C. Leutenantsmeyer, A. A. Kaverzin, M. Wojtaszek, and B. J. van Wees, *2D Materials* **4**, 014001 (2016).
- [17] S. Geprägs, S. Meyer, S. Altmannshofer, M. Opel, F. Wilhelm, A. Rogalev, R. Gross, and S. T. B. Goennenwein, *Applied Physics Letters* , 262407 (2012), <https://doi.org/10.1063/1.4773509>.
- [18] J. Qi, X. Li, Q. Niu, and J. Feng, *Phys. Rev. B* **92**, 121403 (2015).
- [19] L. Xu, M. Yang, L. Shen, J. Zhou, T. Zhu, and Y. P. Feng, *Phys. Rev. B* **97**, 041405 (2018).
- [20] G. Yang, J. Li, H. Ma, Y. Yang, C. Li, X. Mao, and F. Yin, *Phys. Rev. B* **98**, 235419 (2018).
- [21] K. Zollner, P. E. Faria Junior, and J. Fabian, *Phys. Rev. B* **100**, 085128 (2019).
- [22] B. Karpiaĳ, A. W. Cummings, K. Zollner, M. Vila, D. Khokhriakov, A. M. Hoque, A. Dankert, P. Svedlindh, J. Fabian, S. Roche, and S. P. Dash, *2D Materials* **7**, 015026 (2019).
- [23] C. Lee, F. Katmis, P. Jarillo-Herrero, J. S. Moodera, and N. Gedik, *Nature communications* **7**, 1 (2016).
- [24] L. Du, J. Tang, Y. Zhao, X. Li, R. Yang, X. Hu, X. Bai, X. Wang, K. Watanabe, T. Taniguchi, D. Shi, G. Yu, X. Bai, T. Hasan, G. Zhang, and Z. Sun, *Advanced Functional Materials* **29**, 1904734 (2019), <https://onlinelibrary.wiley.com/doi/pdf/10.1002/adfm.201904734>.
- [25] A. Milosavljević, A. Šolajić, J. Pešić, Y. Liu, C. Petrovic, N. Lazarević, and Z. V. Popović, *Phys. Rev. B* **98**, 104306 (2018).
- [26] A. Ghosh, M. Palit, S. Maity, V. Dwij, S. Rana, and S. Datta, *Phys. Rev. B* **103**, 064431 (2021).
- [27] S. Buchenau, S. Scheitz, A. Sethi, J. E. Slimak, T. E. Glier, P. K. Das, T. Dankwort, L. Akinsinde, L. Kienle, A. Rusydi, C. Ulrich, S. L. Cooper, and M. Rübhausen, *Phys. Rev. B* **101**, 245431 (2020).
- [28] B. Irfan, S. Sahoo, A. P. S. Gaur, M. Ahmadi, M. J.-F. Guinel, R. S. Katiyar, and R. Chatterjee, *Journal of Applied Physics* **115**, 173506 (2014), <https://doi.org/10.1063/1.4871860>.
- [29] D. Vaclavkova, M. Palit, J. Wyzula, S. Ghosh, A. Delhomme, S. Maity, P. Kapuscinski, A. Ghosh, M. Veis, M. Grzeszczyk, C. Faugeras, M. Orlita, S. Datta, and M. Potemski, *Phys. Rev. B* **104**, 134437

- (2021).
- [30] M. Koyano, J. Tanaka, K. Suekuni, and T. Ariga, [Journal of electronic materials](#) **41**, 1317 (2012).
- [31] A. Ghosh, M. Birowska, P. K. Ghose, M. Rybak, S. Maity, S. Ghosh, B. Das, S. Bera, S. Bhardwaj, S. Nandi, and S. Datta, [Anisotropic magnetodielectric coupling in layered antiferromagnetic feps<sub>3</sub>](#) (2022).
- [32] A. Castellanos-Gomez, M. Buscema, R. Molenaar, V. Singh, L. Janssen, H. S. J. van der Zant, and G. A. Steele, [2D Materials](#) **1**, 011002 (2014).
- [33] J. Yuan, M. Zhao, W. Yu, Y. Lu, C. Chen, M. Xu, S. Li, K. P. Loh, and Q. Bao, [Materials](#) **8**, 5007 (2015).
- [34] F. Kargar, E. A. Coleman, S. Ghosh, J. Lee, M. J. Gomez, Y. Liu, A. S. Magana, Z. Barani, A. Mohammadzadeh, B. Debnath, *et al.*, [ACS nano](#) **14**, 2424 (2020).
- [35] A. Hashemi, H.-P. Komsa, M. Puska, and A. V. Krasheninnikov, [The Journal of Physical Chemistry C](#) **121**, 27207 (2017).
- [36] J. Menéndez and M. Cardona, [Physical Review B](#) **29**, 2051 (1984).
- [37] P. Mal, G. Bera, G. Turpu, S. K. Srivastava, A. Gangan, B. Chakraborty, B. Das, and P. Das, [Physical Chemistry Chemical Physics](#) **21**, 15030 (2019).
- [38] D. Park, S. Park, K. Jeong, H.-S. Jeong, J. Y. Song, and M.-H. Cho, [Scientific reports](#) **6**, 19132 (2016).
- [39] M. P. Singh, S. Rynthathiang, S. Krishnan, and P. K. Nayak, [Current Chinese Science](#) **1**, 453 (2021).
- [40] P. Klemens, [Physical Review](#) **148**, 845 (1966).
- [41] L. Casto, A. Clune, M. Yokosuk, J. Musfeldt, T. Williams, H. Zhuang, M.-W. Lin, K. Xiao, R. Hennig, B. Sales, *et al.*, [APL materials](#) **3**, 041515 (2015).
- [42] M. Prosnikov, A. Smirnov, V. Y. Davydov, R. Pisarev, N. Lyubochko, and S. Barilo, [Physical Review B](#) **98**, 104404 (2018).
- [43] T. Okuda, K. Nakanishi, S. Miyasaka, and Y. Tokura, [Physical Review B](#) **63**, 113104 (2001).
- [44] E. Lee, J. Ko, J.-Y. Kim, W.-S. Seo, S.-M. Choi, K. H. Lee, W. Shim, and W. Lee, [Journal of Materials Chemistry C](#) **4**, 1313 (2016).
- [45] G. B. Osterhoudt, R. Carelli, K. S. Burch, F. Katmis, N. Gedik, and J. S. Moodera, [Phys. Rev. B](#) **98**, 014308 (2018).
- [46] S. Ghosh and A. Manchon, [Phys. Rev. B](#) **95**, 035422 (2017).
- [47] D. Q. To, W. Wu, S. Bhatt, Y. Liu, A. Janotti, J. M. O. Zide, M. J. H. Ku, J. Q. Xiao, M. B. Jungfleisch, S. Law, and M. F. Doty, [Phys. Rev. Mater.](#) **7**, 045201 (2023).

- [48] C. Wang, X. Zhu, L. Nilsson, J. Wen, G. Wang, X. Shan, Q. Zhang, S. Zhang, J. Jia, and Q. Xue, [Nano Research](#) **6**, 688 (2013).
- [49] D. C. Nguyen, M. Kim, M. Hussain, I. Akhtar, B. A. Naqvi, M. A. Shehzad, J. Jung, Y. Seo, *et al.*, [Nanotechnology](#) **31**, 195701 (2020).
- [50] C. Tang, Z. Zhang, S. Lai, Q. Tan, and W.-b. Gao, [Advanced Materials](#) **32**, 1908498 (2020).
- [51] T. S. Ghiasi, A. A. Kaverzin, A. H. Dismukes, D. K. de Wal, X. Roy, and B. J. van Wees, [Nature nanotechnology](#) **16**, 788 (2021).
- [52] W. Zhu, C. Song, L. Han, H. Bai, C. Chen, and F. Pan, [Phys. Rev. B](#) **108**, L100406 (2023).
- [53] X. Chen, H. Bai, Y. Ji, Y. Zhou, L. Liao, Y. You, W. Zhu, Q. Wang, L. Han, X. Liu, *et al.*, [Nature Electronics](#) **5**, 574 (2022).
- [54] F. Maccherozzi, M. Sperl, G. Panaccione, J. Minár, S. Polesya, H. Ebert, U. Wurstbauer, M. Hochstrasser, G. Rossi, G. Woltersdorf, *et al.*, [Physical review letters](#) **101**, 267201 (2008).
- [55] W. Liu, L. He, Y. Xu, K. Murata, M. C. Onbasli, M. Lang, N. J. Maltby, S. Li, X. Wang, C. A. Ross, *et al.*, [Nano letters](#) **15**, 764 (2015).
- [56] S. Eremeev, V. Men, V. Tugushev, E. V. Chulkov, *et al.*, [Journal of Magnetism and Magnetic Materials](#) **383**, 30 (2015).
- [57] S. Liu, X. Yuan, Y. Zou, Y. Sheng, C. Huang, E. Zhang, J. Ling, Y. Liu, W. Wang, C. Zhang, *et al.*, [npj 2D Materials and Applications](#) **1**, 1 (2017).
- [58] F. Katmis, V. Lauter, F. S. Nogueira, B. A. Assaf, M. E. Jamer, P. Wei, B. Satpati, J. W. Freeland, I. Eremin, D. Heiman, *et al.*, [Nature](#) **533**, 513 (2016).
- [59] H. Wang, Y. Liu, P. Wu, W. Hou, Y. Jiang, X. Li, C. Pandey, D. Chen, Q. Yang, H. Wang, *et al.*, [ACS nano](#) **14**, 10045 (2020).
- [60] W. Zhu, C. Song, L. Han, H. Bai, Q. Wang, S. Yin, L. Huang, T. Chen, and F. Pan, [Advanced Functional Materials](#) **32**, 2108953 (2022).
- [61] A. Ghasemi, D. Kepaptsoglou, P. L. Galindo, Q. M. Ramasse, T. Hesjedal, and V. K. Lazarov, [NPG Asia Materials](#) **9**, e402 (2017).
- [62] P.-C. Yeh, W. Jin, N. Zaki, D. Zhang, J. T. Sadowski, A. Al-Mahboob, A. M. van der Zande, D. A. Chenet, J. I. Dadap, I. P. Herman, P. Sutter, J. Hone, and R. M. Osgood, [Phys. Rev. B](#) **89**, 155408 (2014).
- [63] B. Das, S. Maity, S. Paul, K. Dolui, S. Paramanik, S. Naskar, S. R. Mohanty, S. Chakraborty, A. Ghosh, M. Palit, *et al.*, [ACS nano](#) **15**, 20203 (2021).

- [64] K. Shahil, M. Hossain, V. Goyal, and A. Balandin, *Journal of Applied Physics* **111** (2012).
- [65] K. Shahil, M. Hossain, D. Teweldebrhan, and A. Balandin, *Applied physics letters* **96** (2010).
- [66] J.-U. Lee, S. Lee, J. H. Ryoo, S. Kang, T. Y. Kim, P. Kim, C.-H. Park, J.-G. Park, and H. Cheong, *Nano letters* **16**, 7433 (2016).
- [67] D. Dey, A. Ray, and L. Yu, *Phys. Rev. Mater.* **6**, L061002 (2022).
- [68] K. Zollner, M. Gmitra, T. Frank, and J. Fabian, *Phys. Rev. B* **94**, 155441 (2016).
- [69] J. B. Goodenough, *Phys. Rev.* **100**, 564 (1955).
- [70] J. Kanamori, *Journal of Physics and Chemistry of Solids* **10**, 87 (1959).
- [71] A. Smolyanitsky and V. K. Tewary, *Nanotechnology* **22**, 085703 (2011).
- [72] C. Zhang, M.-Y. Li, J. Tersoff, Y. Han, Y. Su, L.-J. Li, D. A. Muller, and C.-K. Shih, *Nature nanotechnology* **13**, 152 (2018).
- [73] G. Rosenberg and M. Franz, *Phys. Rev. B* **85**, 195119 (2012).
- [74] D. Dey, T. Maitra, U. Waghmare, and A. Taraphder, *Physical Review B* **101**, 205132 (2020).
- [75] P. E. Bl, *Physical Review B* **50**, 953 (1994).
- [76] G. Kresse and D. Joubert, *Physical review b* **59**, 1758 (1999).
- [77] G. Kresse and J. Furthmüller, *Phys. Rev. B* **54**, 11169 (1996).
- [78] G. Kresse and J. Furthmüller, *Computational materials science* **6**, 15 (1996).
- [79] J. P. Perdew, K. Burke, and M. Ernzerhof, *Physical review letters* **77**, 3865 (1996).
- [80] S. L. Dudarev, G. A. Botton, S. Y. Savrasov, C. Humphreys, and A. P. Sutton, *Physical Review B* **57**, 1505 (1998).
- [81] Y. Zheng, X.-x. Jiang, X.-x. Xue, J. Dai, and Y. Feng, *Phys. Rev. B* **100**, 174102 (2019).
- [82] B. L. Chittari, Y. Park, D. Lee, M. Han, A. H. MacDonald, E. Hwang, and J. Jung, *Phys. Rev. B* **94**, 184428 (2016).
- [83] D. Dey, T. Maitra, and A. Taraphder, *Physical Review B* **93**, 195133 (2016).
- [84] S. Baroni, S. De Gironcoli, A. Dal Corso, and P. Giannozzi, *Reviews of modern Physics* **73**, 515 (2001).
- [85] A. Togo and I. Tanaka, *Scripta Materialia* **108**, 1 (2015).
- [86] S. Smidstrup, T. Markussen, P. Vancraeyveld, J. Wellendorff, J. Schneider, T. Gunst, B. Verstichel, D. Stradi, P. A. Khomyakov, U. G. Vej-Hansen, *et al.*, *Journal of Physics: Condensed Matter* **32**, 015901 (2019).
- [87] D. Stradi, L. Jelver, S. Smidstrup, and K. Stokbro, *Journal of Physics: Condensed Matter* **29**, 185901

(2017).

[88] S. Grimme, J. Antony, S. Ehrlich, and H. Krieg, *The Journal of chemical physics* **132**, 154104 (2010).

[89] M. Pajda, J. Kudrnovský, I. Turek, V. Drchal, and P. Bruno, *Phys. Rev. B* **64**, 174402 (2001).

[90] J. P. Perdew, K. Burke, and M. Ernzerhof, *Phys. Rev. Lett.* **77**, 3865 (1996).

[91] M. van Setten, M. Giantomassi, E. Bousquet, M. Verstraete, D. Hamann, X. Gonze, and G.-M. Rignanese, *Computer Physics Communications* **226**, 39 (2018).

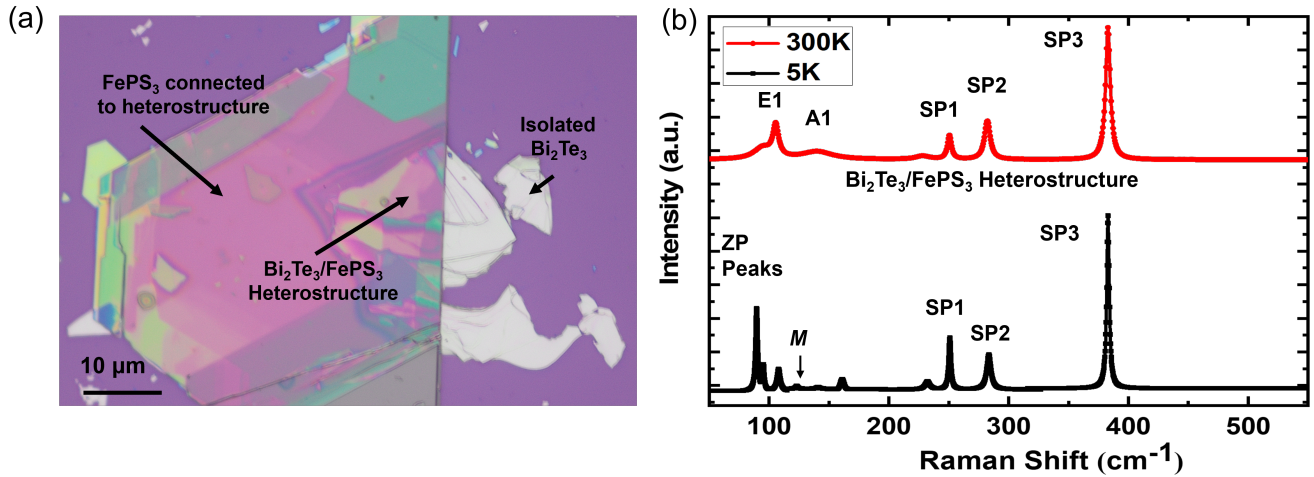


FIG. 1. (a) Optical microscopy image of heterostructure (HS-1) fabricated *via* stamping method onto a 300 nm Si/SiO<sub>2</sub> substrate. Raman spectroscopy of (b) Bi<sub>2</sub>Te<sub>3</sub>/FePS<sub>3</sub> heterostructure (HS-1) at 5 K and room temperature obtained with an excitation wavelength 473 nm. Spin-phonon coupled peaks and Magnon Peak are designated as SP(1-3) and *M* respectively. Zone folded phonon modes (ZPs) appear at low temperature is not present at room temperature. Individual characteristics phonon modes of Bi<sub>2</sub>Te<sub>3</sub> (denoted as E1 and A1) and FePS<sub>3</sub> are present in Bi<sub>2</sub>Te<sub>3</sub>/FePS<sub>3</sub> heterostructure.

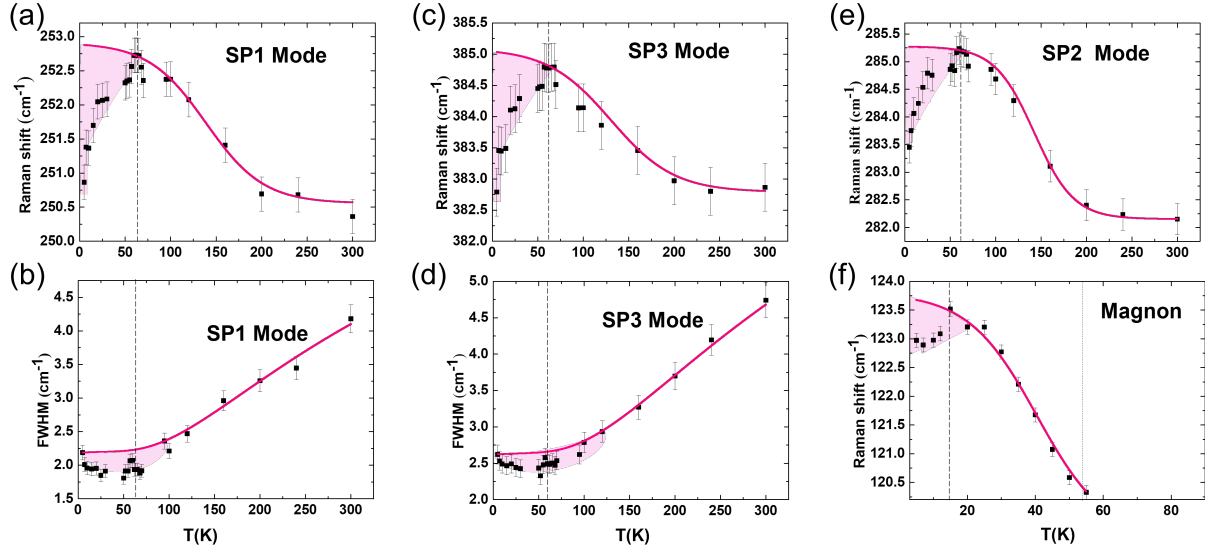


FIG. 2. Variation of Peak position and linewidth of FePS<sub>3</sub> Raman modes (a), (b) SP1 mode; (c), (d) SP3 mode; (e) SP2 mode (f) Magnon mode in the heterostructure (HS-1) with temperature. All spin-phonon peaks show phonon anomaly at around 65 K in phonon frequency. At below 65 K, linewidths of all spin-phonon mode of FePS<sub>3</sub> are not fit with 3-phonon Anharmonic Decay (AD) model due to presence of Bi<sub>2</sub>Te<sub>3</sub> underneath. One-magnon mode [Fig.(f)] at 120 cm<sup>-1</sup> at a temperature ( $T_M \sim 60$  K) was observed in FePS<sub>3</sub>. Softening of this magnon mode was observed with the temperature and the softening temperature becomes half due to Bi<sub>2</sub>Te<sub>3</sub> underneath.

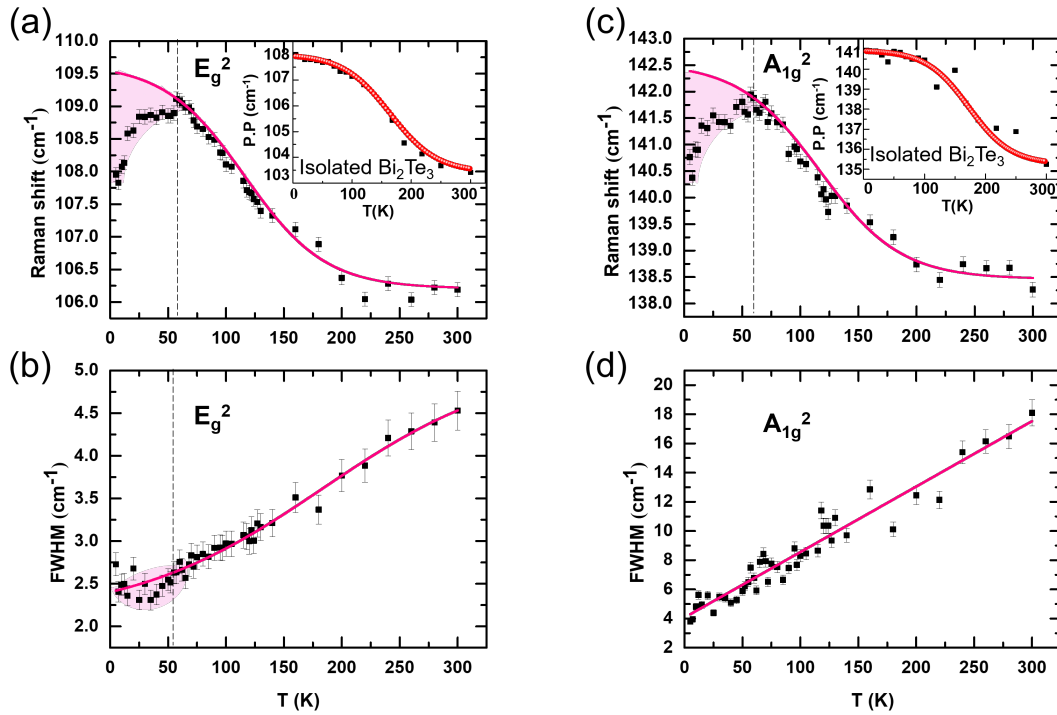


FIG. 3. Variation of peak position and linewidth of Raman modes of Bi<sub>2</sub>Te<sub>3</sub> in the heterostructure (HS-1) (a),(b) In-plane Raman mode E<sub>g</sub><sup>2</sup>; (c),(d) Out-of-plane Raman mode A<sub>1g</sub><sup>2</sup> of Bi<sub>2</sub>Te<sub>3</sub> with temperature. Insets (a), (c) showing the temperature dependence of Raman modes of isolated Bi<sub>2</sub>Te<sub>3</sub>. No phonon anomaly was observed in the in-plane and out-of-plane Raman modes of isolated Bi<sub>2</sub>Te<sub>3</sub>. In case of Bi<sub>2</sub>Te<sub>3</sub> in the heterostructure (HS-1), phonon anomaly was observed in both Raman modes of Bi<sub>2</sub>Te<sub>3</sub> in phonon frequency at around 60 K. Linewidth of in-plane Raman mode [Fig (b)] of Bi<sub>2</sub>Te<sub>3</sub> was not fit by Boltzmann sigmoidal anharmonic curve at/below 60 K. Linewidth of out-of-plane Raman mode of Bi<sub>2</sub>Te<sub>3</sub> [Fig(d)] increases with the temperature in the whole temperature window.



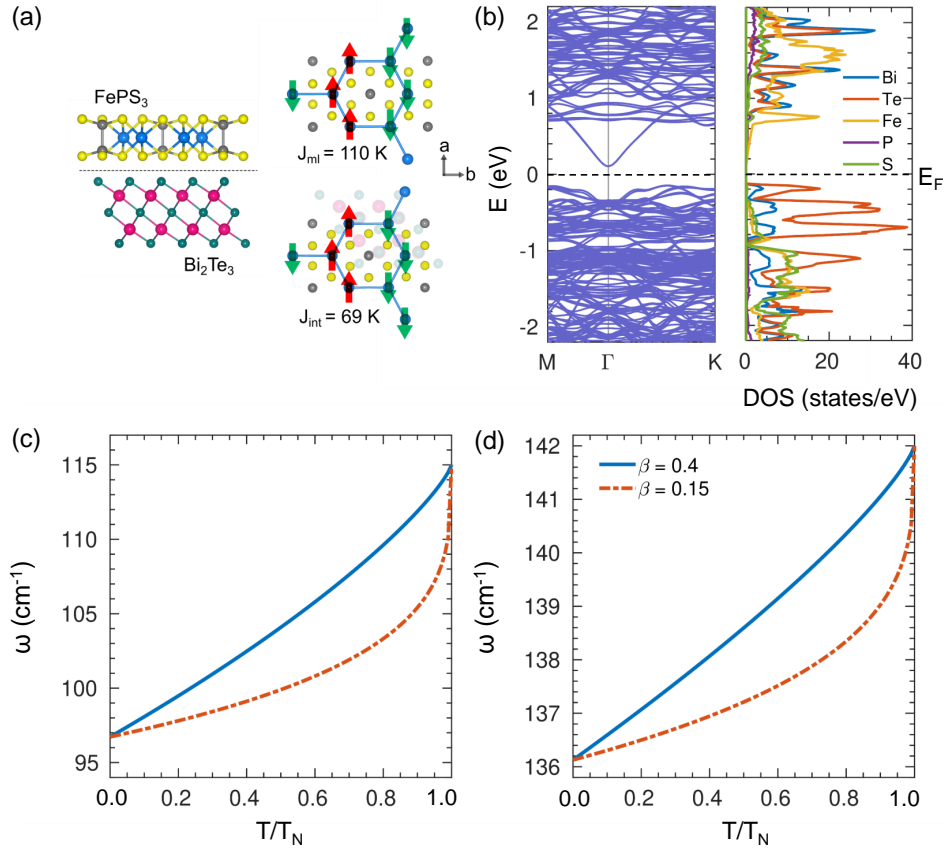


FIG. 4. (a) A schematic of Bi<sub>2</sub>Te<sub>3</sub>/FePS<sub>3</sub> heterostructure and the zigzag AFM order of an isolated FePS<sub>3</sub> monolayer and a monolayer on top of Bi<sub>2</sub>Te<sub>3</sub>. The respective AFM exchange values are also shown. (b) Band structure and atom projected density of states (DOS) of Bi<sub>2</sub>Te<sub>3</sub>/FePS<sub>3</sub> heterostructure obtained within GGA+U+SOC reveal that the system is a narrow band gap semiconductor. Temperature dependence of (c) 115 cm<sup>-1</sup> and (d) 141 cm<sup>-1</sup> FePS<sub>3</sub> phonon modes that are coupled to Bi<sub>2</sub>Te<sub>3</sub> modes are shown for two critical exponent ( $\beta$ ) values obtained from experiments.

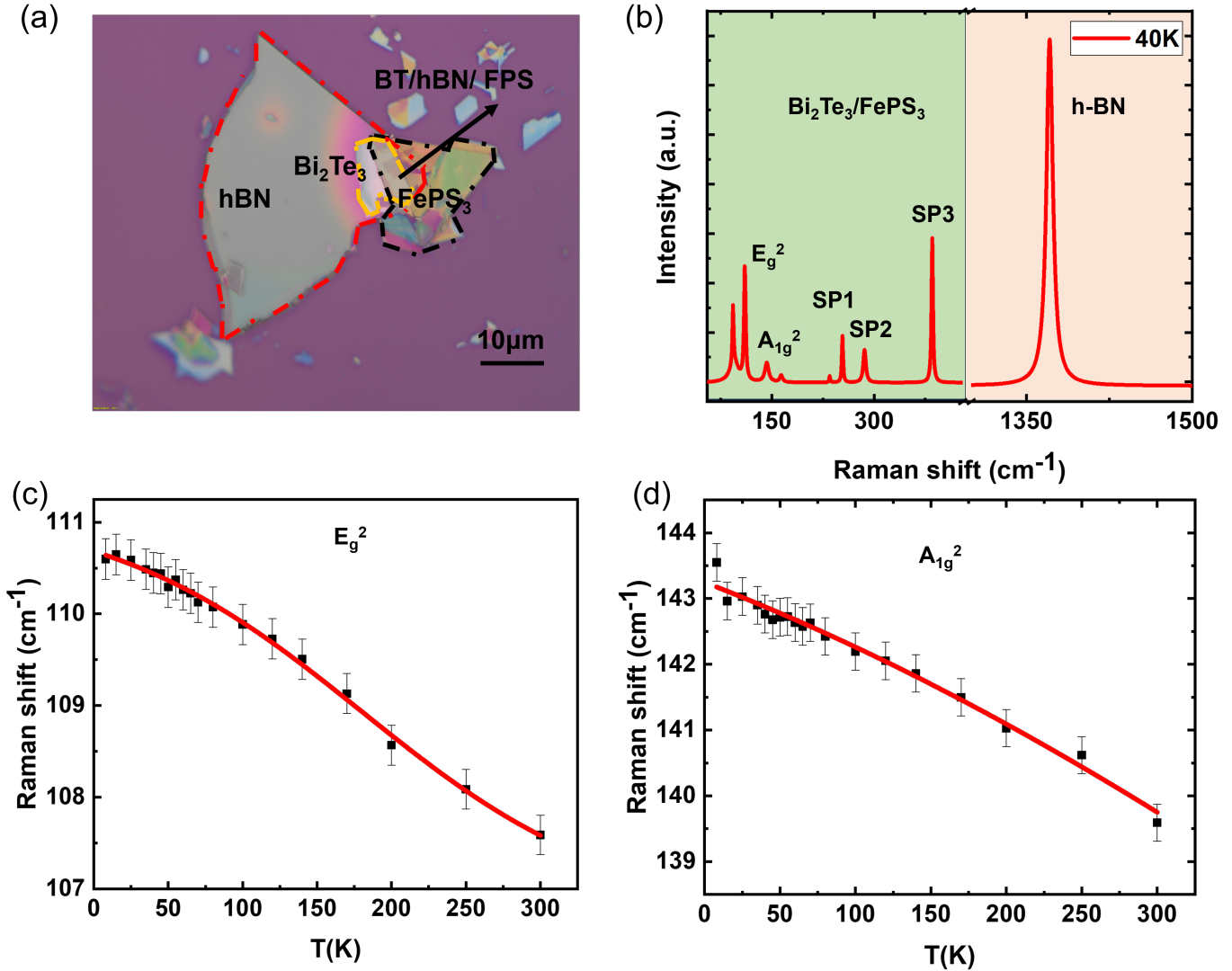


FIG. 5. (a) Optical microscopy image of heterostructure (HS-4). Orange dotted line surrounds Bi<sub>2</sub>Te<sub>3</sub> flake. Bulk hBN (red dotted line) is first placed on top of Bi<sub>2</sub>Te<sub>3</sub>. FePS<sub>3</sub> (black dotted line) covers both Bi<sub>2</sub>Te<sub>3</sub> (some portion) and hBN (some portion) resulting the formation of Bi<sub>2</sub>Te<sub>3</sub>/hBN/ FePS<sub>3</sub> heterostructure. (b) Raman spectra of the heterostructure (HS-4) at low temperature. Individual Raman modes of Bi<sub>2</sub>Te<sub>3</sub>, hBN and FePS<sub>3</sub> are appeared in Bi<sub>2</sub>Te<sub>3</sub>/hBN/ FePS<sub>3</sub> heterostructure. Variation of peak position of Raman modes of Bi<sub>2</sub>Te<sub>3</sub> (c) In-plane Raman mode E<sub>g</sub><sup>2</sup>; (d) Out-of-plane Raman mode A<sub>1g</sub><sup>2</sup> of Bi<sub>2</sub>Te<sub>3</sub> with temperature in the heterostructure (figure (a)). No phonon anomaly was observed in the in-plane and out-of-plane Raman modes of Bi<sub>2</sub>Te<sub>3</sub> due to the presence of hBN like isolated one.

# Supplementary Information: Manipulating Spin-Lattice Coupling in Layered Magnetic Topological Insulator Heterostructure *via* Interface Engineering

Sujan Maity,<sup>1</sup> Dibyendu Dey,<sup>2</sup> Anudeepa Ghosh,<sup>1</sup> Suvadip Masanta,<sup>3</sup> Binoy Krishna De,<sup>4</sup> Hemant Singh Kunwar,<sup>4</sup> Bikash Das,<sup>1</sup> Tanima Kundu,<sup>1</sup> Mainak Palit,<sup>1</sup> Satyabrata Bera,<sup>1</sup> Kapildeb Dolui,<sup>5</sup> Kenji Watanabe,<sup>6</sup> Takashi Taniguchi,<sup>7</sup> Liping Yu,<sup>2</sup> A Taraphder,<sup>8</sup> and Subhadeep Datta\*<sup>1</sup>

<sup>1</sup>*School of Physical Sciences, Indian Association for the Cultivation of Science,  
2A & 2B Raja S. C. Mullick Road, Jadavpur, Kolkata - 700032, India*

<sup>2</sup>*Department of Physics and Astronomy,  
University of Maine, Orono, ME 04469, USA*

<sup>3</sup>*Bose Institute, Department of Physics Main Campus 93/1,  
A. P. C. Road Kolkata - 700 009, India*

<sup>4</sup>*UGC-DAE Consortium for Scientific Research, Indore Centre,  
University Campus, Khandwa Road, Indore 452001*

<sup>5</sup>*Lomare Technolgies Limited, 6 London Street, London EC3R 7LP, United Kingdom*

<sup>6</sup>*Research Center for Functional Materials,  
National Institute for Materials Science, Tsukuba 305-0044, Japan*

<sup>7</sup>*International Center for Materials Nanoarchitectonics,  
National Institute for Materials Science, Tsukuba 305-0044, Japan*

<sup>8</sup>*Department of Physics, Indian Institute of Technology Kharagpur, W.B. 721302, India*

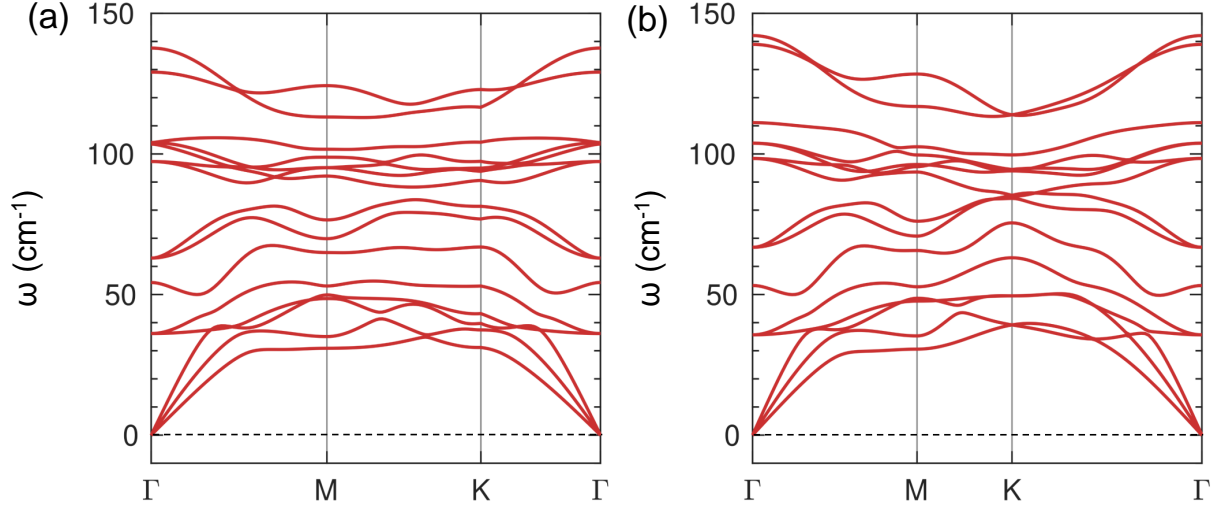


FIG. S1. Phonon dispersion of  $\text{Bi}_2\text{Te}_3$  (a) bulk and (b) monolayer structures, respectively. The phonon dispersion of  $\text{Bi}_2\text{Te}_3$  monolayer agree well with its bulk counterpart. No imaginary frequencies have been observed in phonon dispersion, suggesting that this structure is dynamically stable.

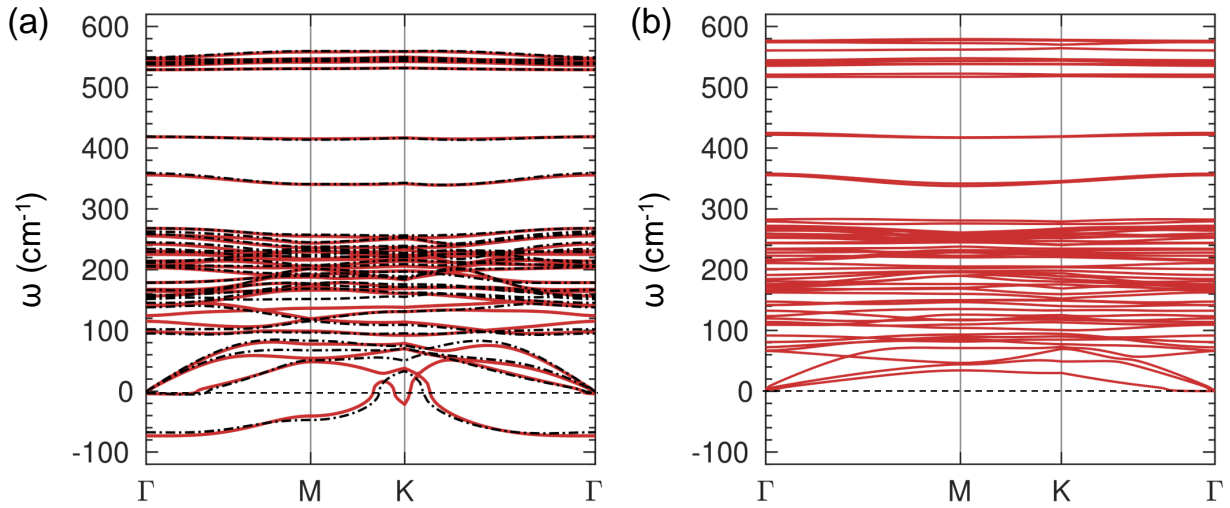


FIG. S2. (a) Phonon dispersion of  $\text{FePS}_3$  monolayer for z-AFM (red solid lines) and FM (black dotted lines) spin configurations in the experimentally reported point-group structure. (b) Phonon dispersion of distorted  $\text{FePS}_3$  monolayer for z-AFM spin configuration indicate the dynamical stability due to the absence of imaginary modes

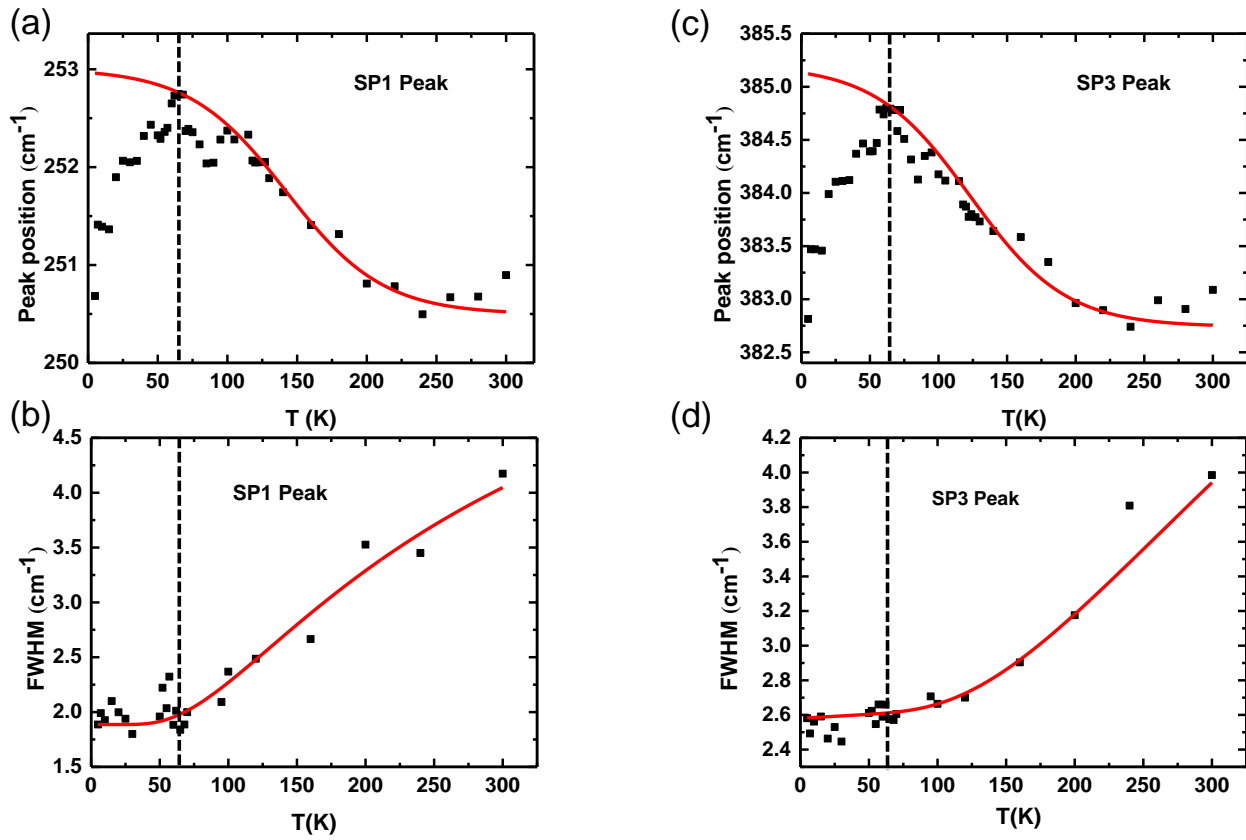


FIG. S3. Variation of Peak position and linewidth of FePS<sub>3</sub> Raman modes connected to heterostructure with temperature. (a),(b) SP1 mode; (c), (d) SP3 mode; All spin-phonon peaks show phonon anomaly at around 65 K in phonon frequency. Linewidths of all spin-phonon mode of FePS<sub>3</sub> are fit with 3-phonon anharmonic decay (AD) model.

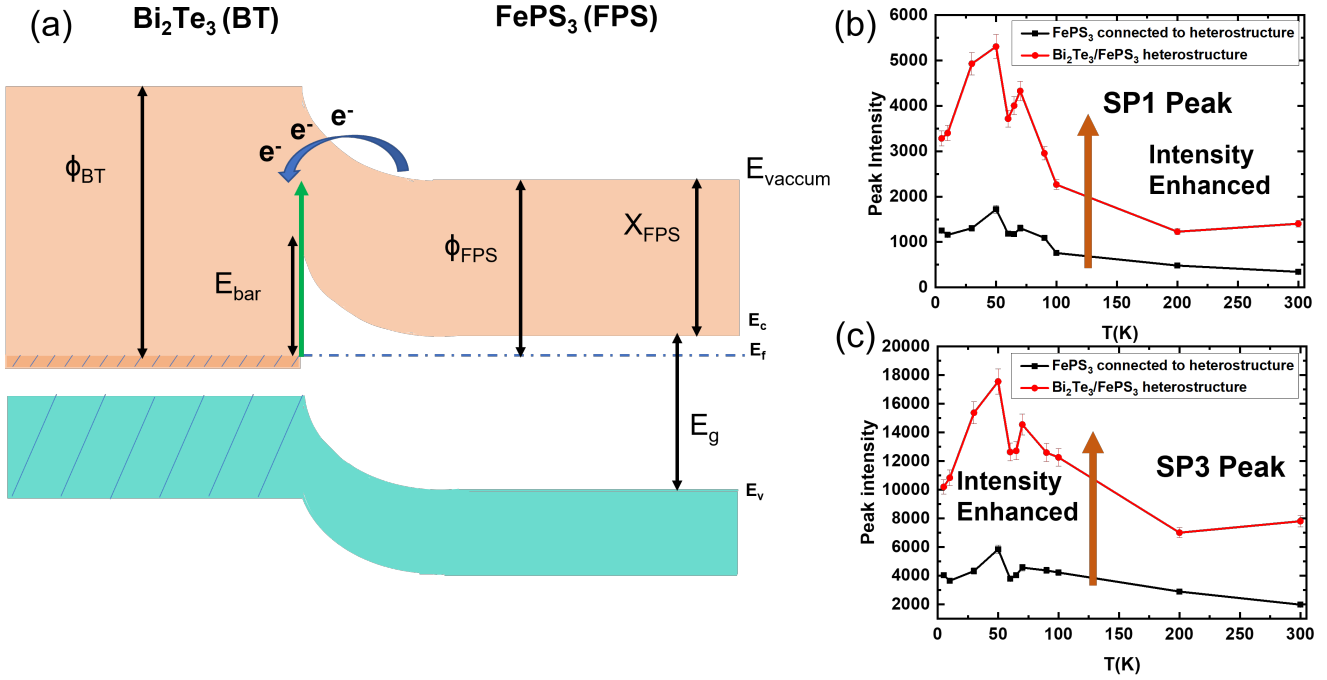


FIG. S4. (a) Schematic diagram of the band bending that occurs at the interface between the metallic Bi<sub>2</sub>Te<sub>3</sub> and the semiconducting FePS<sub>3</sub>. The work function of Bi<sub>2</sub>Te<sub>3</sub> ( $\phi_{Bi_2Te_3} = 5.30$  eV) is larger than that of FePS<sub>3</sub> ( $\phi_{FePS_3} = 4.23$  eV) which leads to the formation of a Schottky barrier of height  $\phi_{Bi_2Te_3} - \chi_{FePS_3} = 1.17$  eV at the interface. To balance out the chemical potential electrons move from the FePS<sub>3</sub> into the Bi<sub>2</sub>Te<sub>3</sub>. (b), (c) Intensity of Raman peaks of FePS<sub>3</sub> are enhanced due to Bi<sub>2</sub>Te<sub>3</sub> underneath compare to isolated FePS<sub>3</sub> Raman modes. In Bi<sub>2</sub>Te<sub>3</sub>-FePS<sub>3</sub> heterostructure, barrier height ( $E_{bar}$ ) (1.17 eV) < Raman excitation (denoted by green arrow) (2.62 eV). The available transitions for Raman scattering will then involve real energy levels, drastically enhancing the intensity

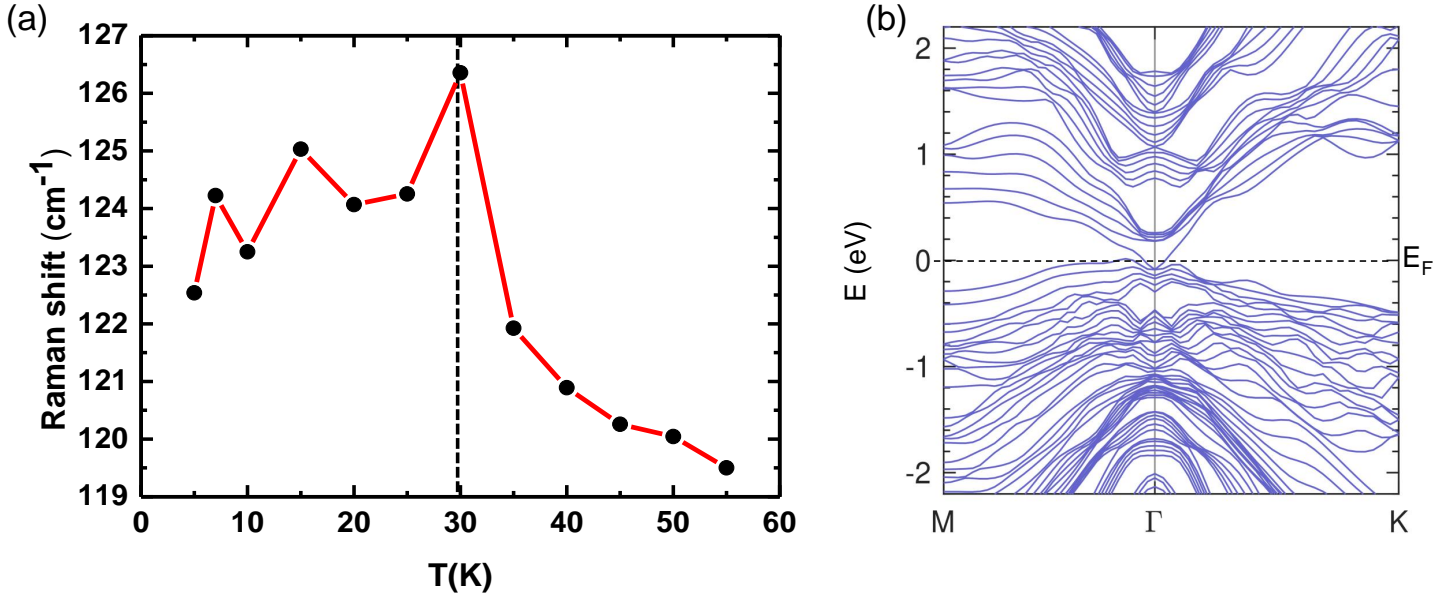


FIG. S5. (a) Magnon mode of  $\text{FePS}_3$  connected to heterostructure. One-magnon mode at  $120 \text{ cm}^{-1}$  at a temperature ( $T_M \sim 60\text{K}$ ) was observed in  $\text{FePS}_3$ . Softening of this magnon mode was observed with the temperature and the softening temperature is 30K in case of  $\text{FePS}_3$ . (b) Electronic structure of 6 quintuple layers of  $\text{Bi}_2\text{Te}_3$ . Metallic surface states start appearing at a thickness ( $\sim 6 \text{ nm}$ ) of 6 quintuple layers.

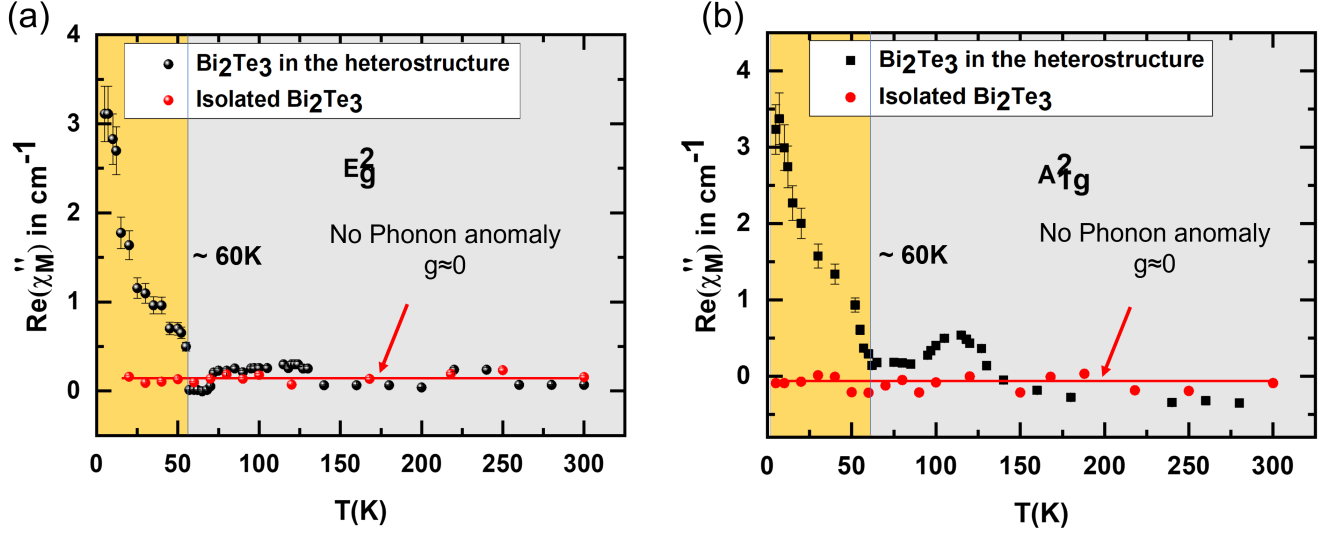


FIG. S6. Real part of Magnetic Susceptibility of (a) In-plane  $E_g^2$  mode; (b) Out-of-plane  $A_{1g}^2$  mode of  $\text{Bi}_2\text{Te}_3$  in  $\text{Bi}_2\text{Te}_3/\text{FePS}_3$  heterostructure ; No such change in spin-phonon coupling constant ( $g$ ) was observed with temperature in both Raman modes of isolated  $\text{Bi}_2\text{Te}_3$  due to pure phononic behaviour in the whole temperature range. In case of  $\text{Bi}_2\text{Te}_3$ , in the heterostructure, slope of the curve changes around 60K and this is the reflection of proximity induced spin-phonon coupling of  $\text{Bi}_2\text{Te}_3$ , occurs at/around 60K.

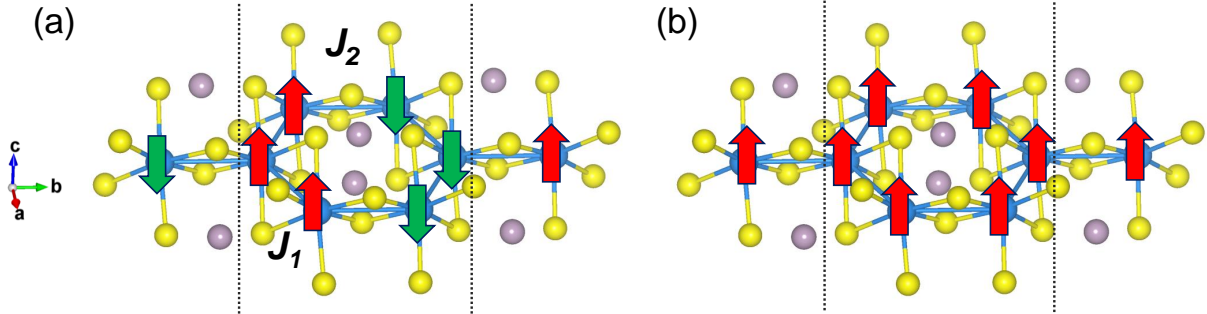


FIG. S7. (a) zig-zag AFM and (b) FM spin configurations of  $\text{FePS}_3$  monolayer that are used to evaluate Fe-Fe AFM exchange.

By mapping the DFT total energy of z-AFM ( $E_1$ ) and FM spin configurations ( $E_2$ ) to the Heisenberg spin model,  $H = J \sum_{i>j} S_i \cdot S_j$ , we obtain the following equations-

$$E_1 = 4J_1S^2 - 2J_2S^2 + \epsilon \quad (1)$$



$$E_2 = 4J_1S^2 + 2J_2S^2 + \epsilon \quad (2)$$

$$J_2 = \frac{(E_2 - E_1)}{4S^2} \quad (3)$$

where,  $J_1$  is the FM exchange along the a-axis and  $J_2$  is the AFM exchange along the b-axis. Stronger  $J_2$  indicates higher  $T_N$ , whereas weaker  $J_2$  indicates lower  $T_N$ .

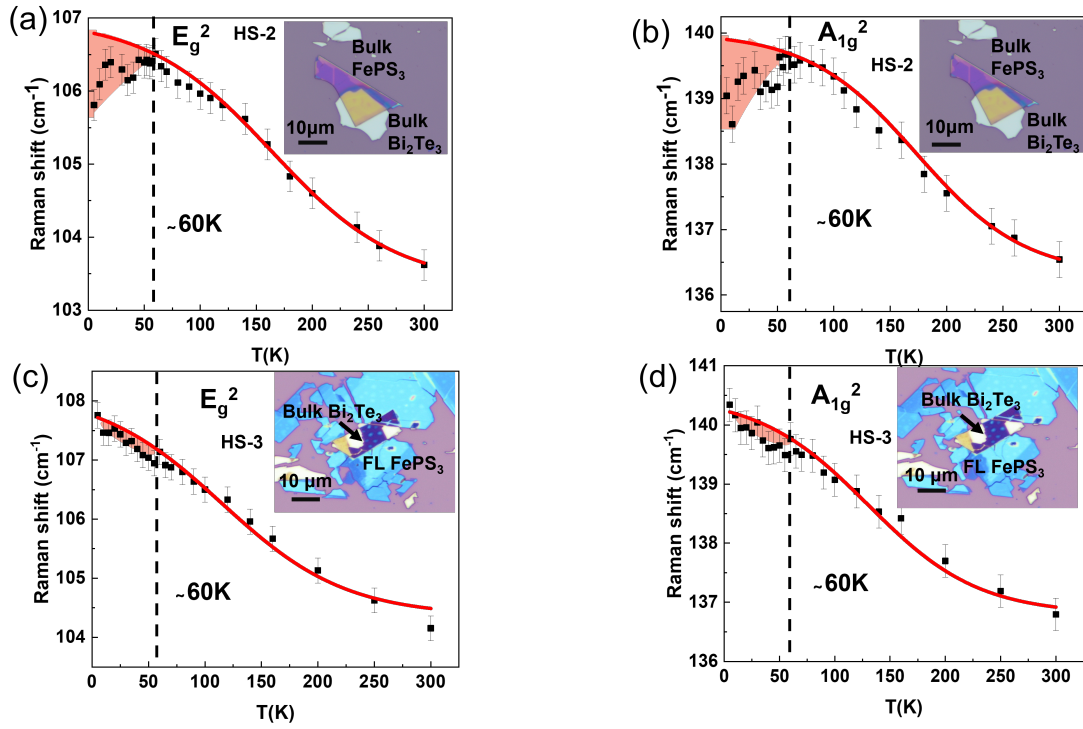


FIG. S8. Thickness dependent Raman studies on Bi<sub>2</sub>Te<sub>3</sub>/FePS<sub>3</sub> heterostructure with temperature.(a) In-plane phonon mode ( $E_g^2$ ) and (b) Out-of-plane phonon mode ( $A_{1g}^2$ ) of Bi<sub>2</sub>Te<sub>3</sub> in bulk Bi<sub>2</sub>Te<sub>3</sub> / bulk FePS<sub>3</sub> heterostructure (HS-2) and, (c) In-plane phonon mode ( $E_g^2$ ) and (d) Out-of-plane phonon mode ( $A_{1g}^2$ ) of Bi<sub>2</sub>Te<sub>3</sub> in bulk Bi<sub>2</sub>Te<sub>3</sub>/Few layer FePS<sub>3</sub> heterostructure (HS-3). Insets are showing the optical microscopy images of HS-2 and HS-3. The deviation from anharmonic behaviour,  $\Delta\omega$  (related to square of magnetization) values for HS-2 and HS-3 heterostructures, are 0.69 and 0.57 respectively for both phonon modes of Bi<sub>2</sub>Te<sub>3</sub>. Strength of the spin-phonon coupling decreases but phonon anomaly in both Raman modes of Bi<sub>2</sub>Te<sub>3</sub> remains invariant ( $\sim 60$ K) with reduction of thickness of the heterostructures.

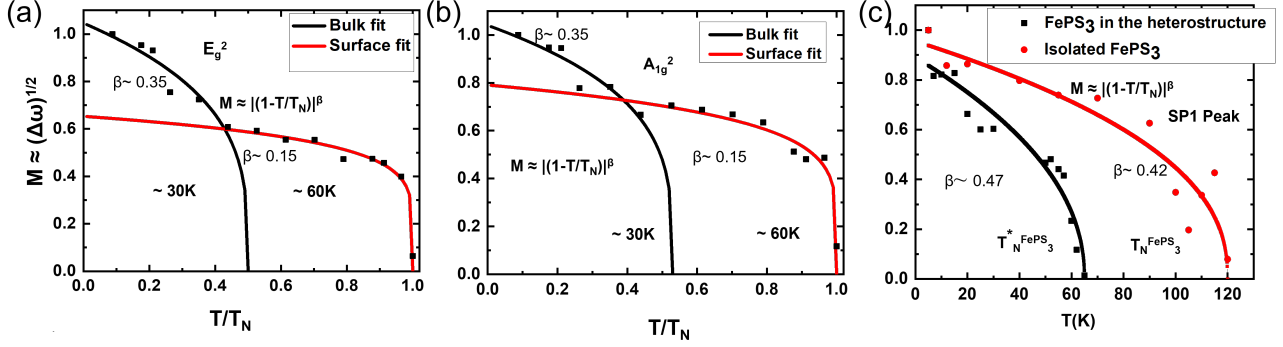


FIG. S9. Antiferromagnetic order parameter of (a) In plane  $E_g^2$  mode; (b) out of plane  $A_{1g}^2$  mode of  $\text{Bi}_2\text{Te}_3$  in the heterostructure ; (c) SP1 peak for two different configurations,  $\text{FePS}_3$  in the heterostructure ( $T_N^*$ ) and isolated  $\text{FePS}_3$  ( $T_N$ ) respectively as a function of temperature. Data points are fit with  $M \approx |(1 - \frac{T}{T_N})|^\beta$  equation.  $\beta$  is the critical exponent. The  $\beta$  value at 60K (0.15) for surface magnetism corroborates the value of 2D Ising model. The  $\beta$  value at 30K (0.35) corresponds to 3D Heisenberg model, responsible for bulk contribution. The  $\beta$  values for the  $\text{FePS}_3$  [Fig (c)] are close to mean field value.

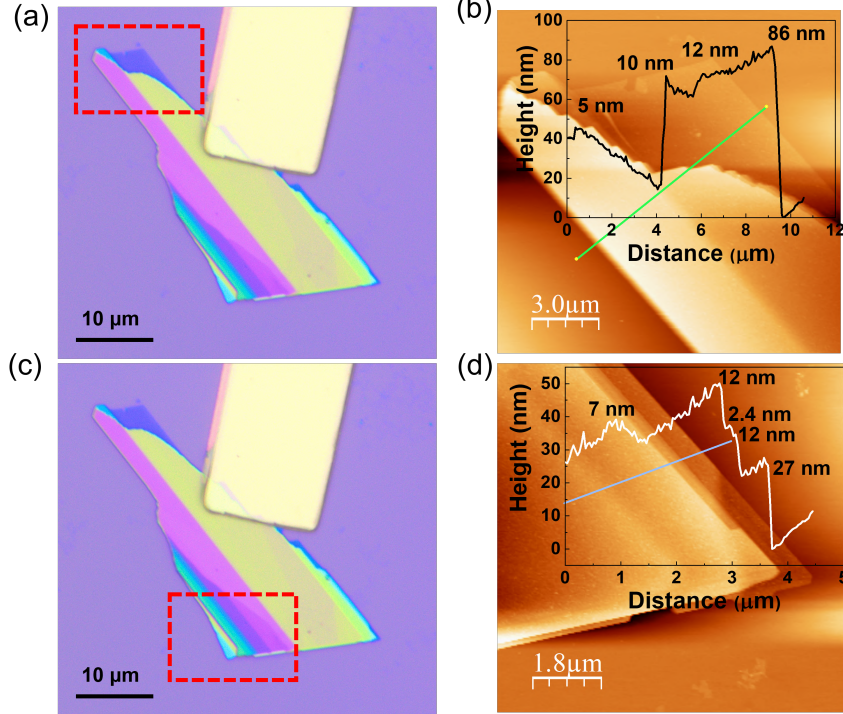


FIG. S10. (a), (c) Optical microscopy image of  $\text{FePS}_3$  flake 1. (b), (d) Atomic force microscopy images of the highlighted area of the flake 1. Insets of (b), (d) show the height profile of the flake.

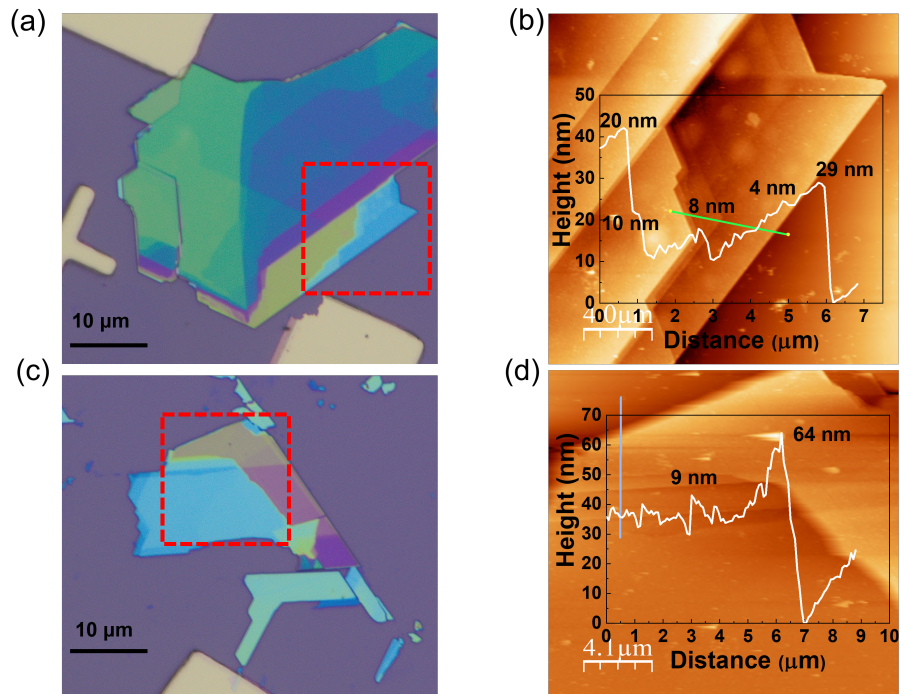


FIG. S11. (a), (c) Optical microscopy image of FePS<sub>3</sub> flake 2 and flake 3. (b), (d) Atomic force microscopy images of the highlighted area of the flake 2 and 3. Insets of (b), (d) show the height profile of the flakes.

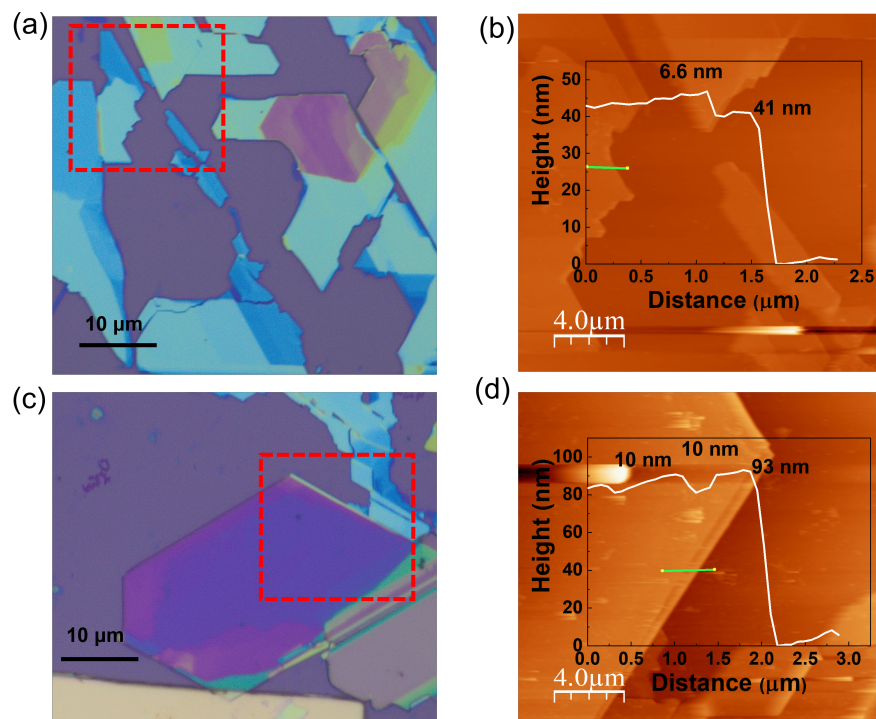


FIG. S12. (a), (c) Optical microscopy image of FePS<sub>3</sub> flake 4 and flake 5. (b), (d) Atomic force microscopy images of the highlighted area of the flake 4 and flake 5. Insets of (b), (d) show the height profile of the flakes.

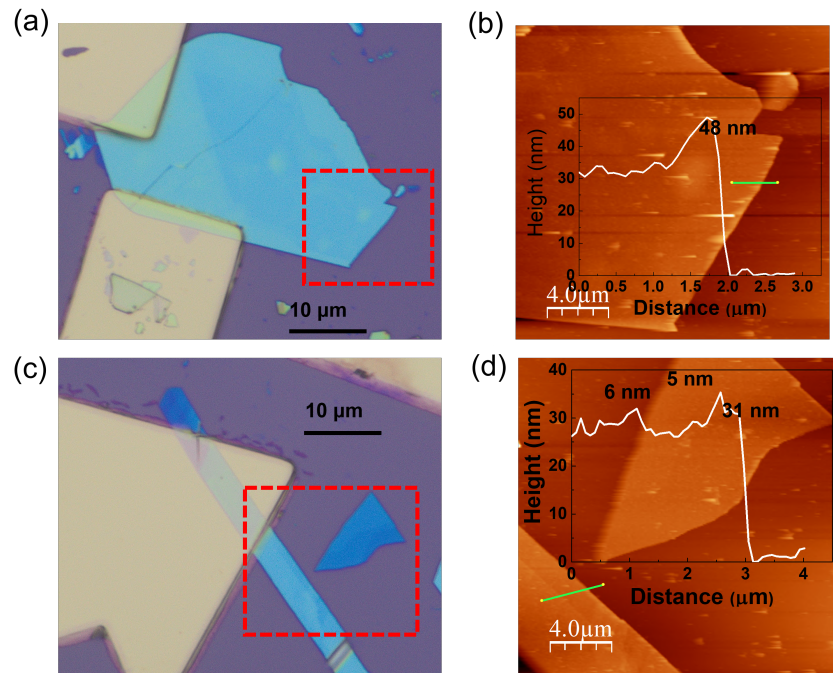


FIG. S13. (a), (c) Optical microscopy image of FePS<sub>3</sub> flake 6 and flake 7. (b), (d) Atomic force microscopy images of the highlighted area of the flake 6 and flake 7. Insets of (b), (d) show the height profile of the flakes.

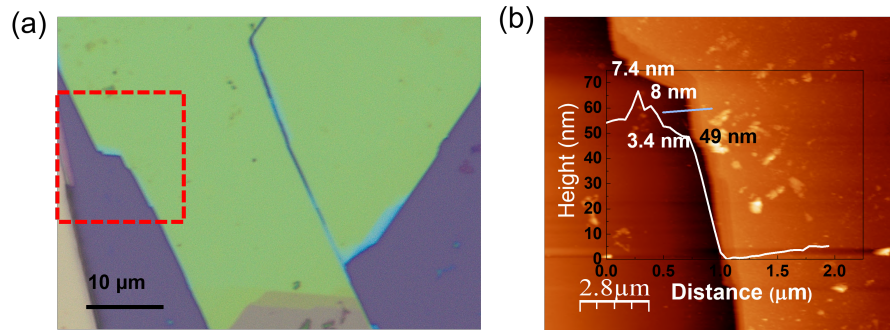


FIG. S14. (a) Optical microscopy image of FePS<sub>3</sub> flake 8. (b) Atomic force microscopy image of the highlighted area of the flake 8. Inset of (b) shows the height profile of the flake.

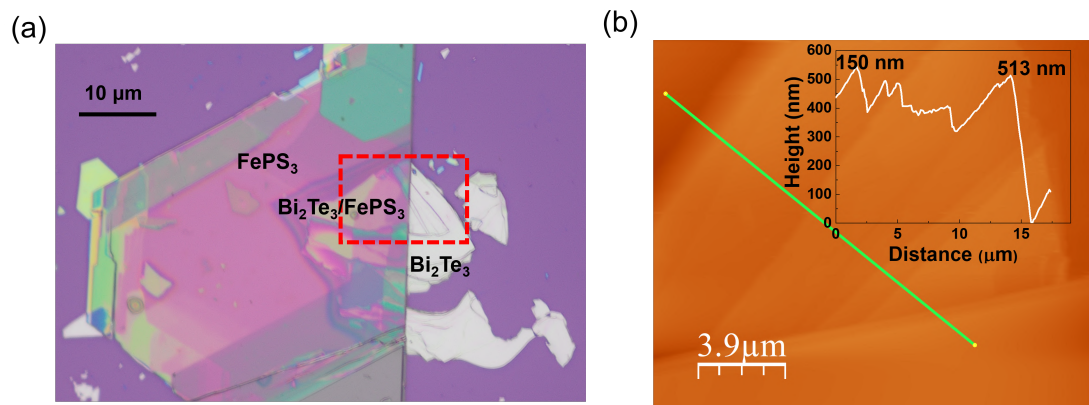


FIG. S15. (a) Optical microscopy image of Bi<sub>2</sub>Te<sub>3</sub>/FePS<sub>3</sub> heterostructure (HS-1). (b) Atomic force microscopy image of Bi<sub>2</sub>Te<sub>3</sub>/FePS<sub>3</sub> (HS-1). Inset of (b) shows the height profile of the heterostructure.

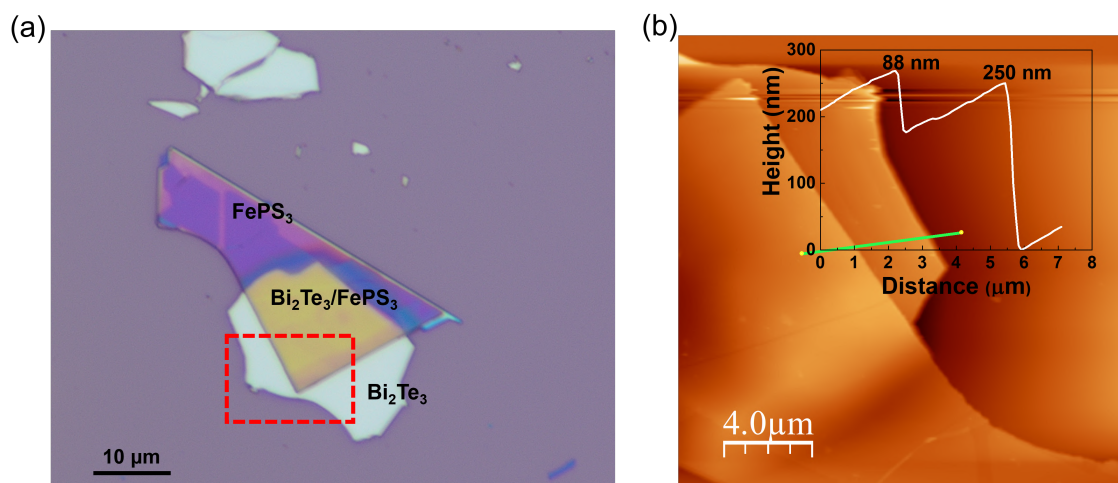


FIG. S16. (a) Optical microscopy image of Bi<sub>2</sub>Te<sub>3</sub>/FePS<sub>3</sub> (HS-2). (b) Atomic force microscopy image of Bi<sub>2</sub>Te<sub>3</sub>/FePS<sub>3</sub> (HS-2). Inset of (b) shows the height profile of the heterostructure.

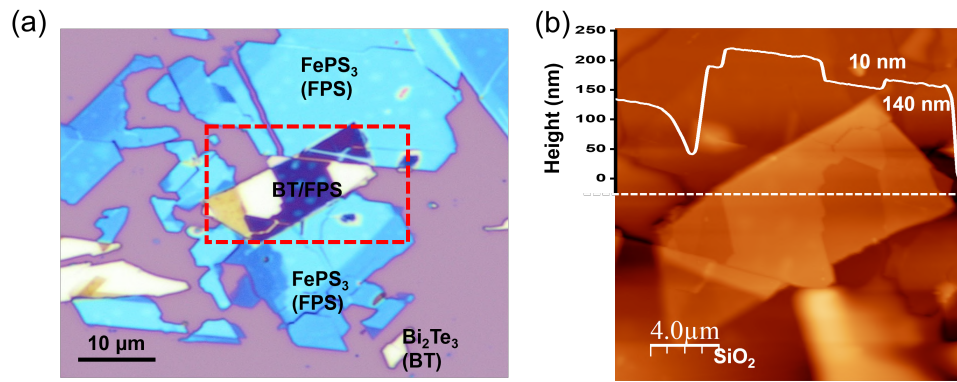


FIG. S17. (a) Optical microscopy image of  $\text{Bi}_2\text{Te}_3/\text{FePS}_3$  (HS-3). (b) Atomic force microscopy image of  $\text{Bi}_2\text{Te}_3/\text{FePS}_3$  (HS-3). Inset of (b) shows the height profile of the heterostructure.

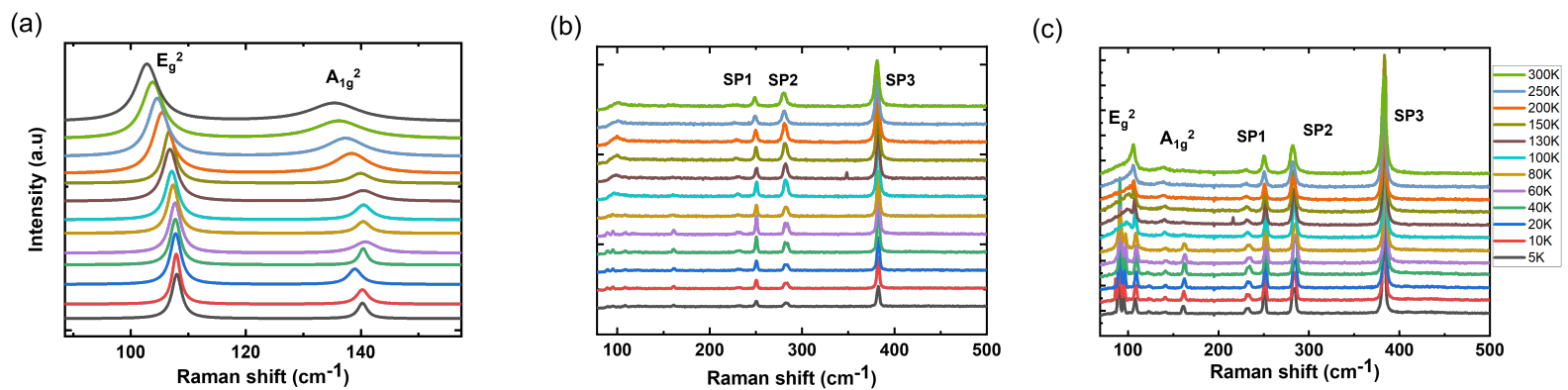


FIG. S18. Raman spectra of (a) isolated  $\text{Bi}_2\text{Te}_3$ , (b) isolated  $\text{FePS}_3$ , (c)  $\text{Bi}_2\text{Te}_3/\text{FePS}_3$  heterojunction of multiple sampling points at different temperature (5K to 300K)

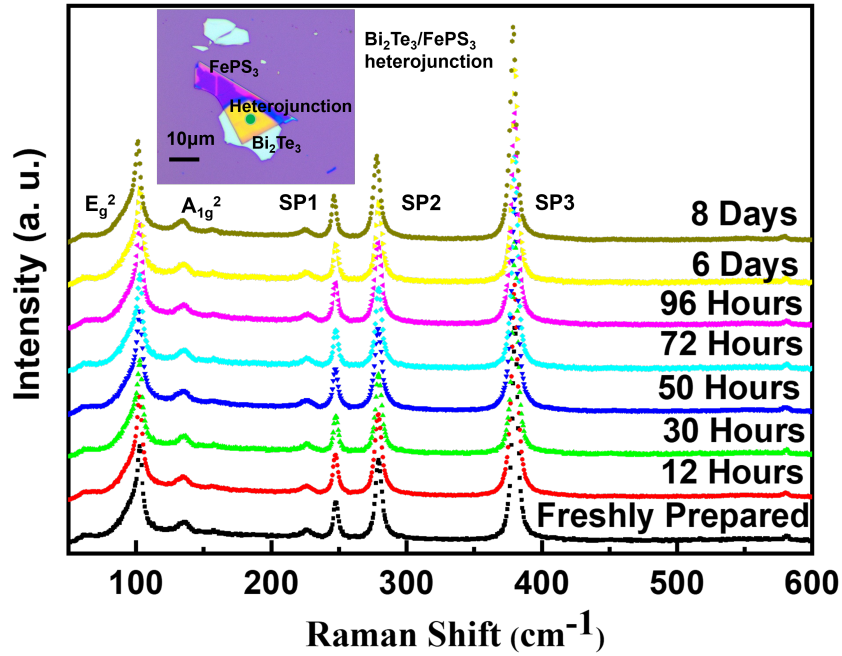


FIG. S19. Raman Spectra of  $\text{Bi}_2\text{Te}_3/\text{FePS}_3$  heterojunction were recorded for 8 days to check the air stability of the heterostructure. Inset shows the optical microscopy image of the heterostructure. Green dot in heterojunction signifies the laser spot. No change was observed in peak position and linewidth of  $\text{Bi}_2\text{Te}_3$  and  $\text{FePS}_3$  Raman modes.

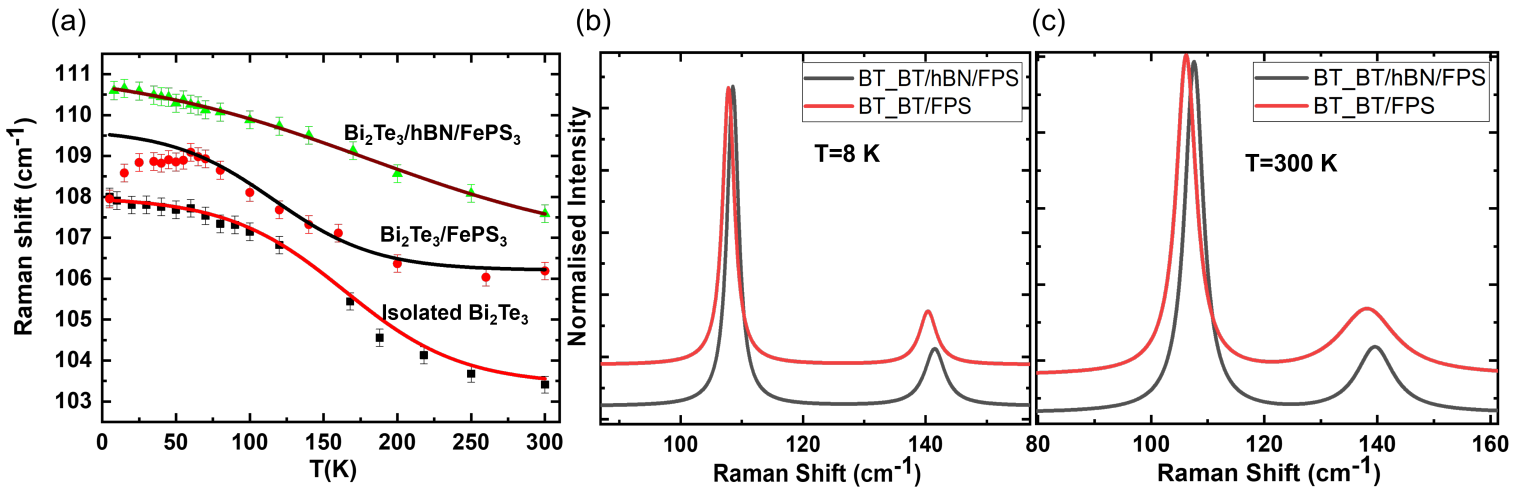


FIG. S20. (a) Variation of in-plane Raman modes of  $\text{Bi}_2\text{Te}_3$  are plotted with temperature for isolated and for different heterostructures; (b), (c) Raman shifts of  $\text{Bi}_2\text{Te}_3$  modes are shown for two different temperatures in heterostructures.



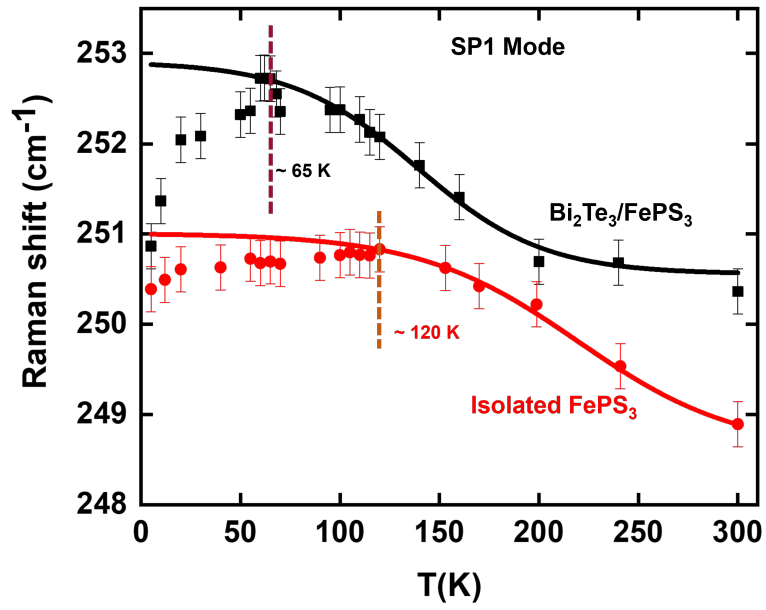


FIG. S21. Variation of FePS<sub>3</sub> spin-phonon coupled mode (SP1) with temperature for two different configurations. In case of isolated FePS<sub>3</sub>, the characteristic Néel temperature ( $T_N$ ) is around 120 K and reduction of  $T_N$  was observed at/around 65 K due to Bi<sub>2</sub>Te<sub>3</sub> underneath in heterostructure.

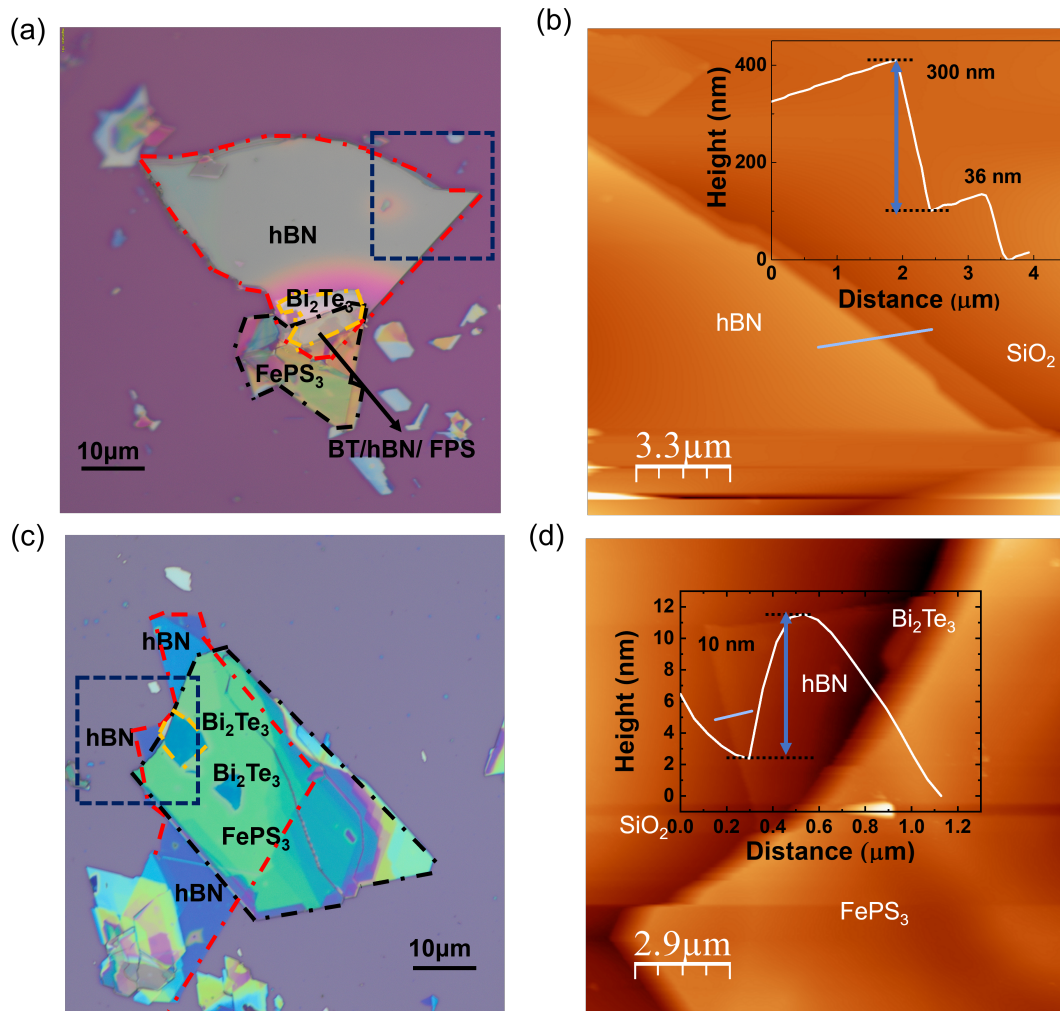


FIG. S22. (a), (c) Optical microscopy images of  $\text{Bi}_2\text{Te}_3/\text{hBN}/\text{FePS}_3$  HS with two different thickness of  $\text{hBN}$ . (b),(d) Atomic force microscopy images of HS. Insets of (b), (d) show the height profile of  $\text{hBN}$

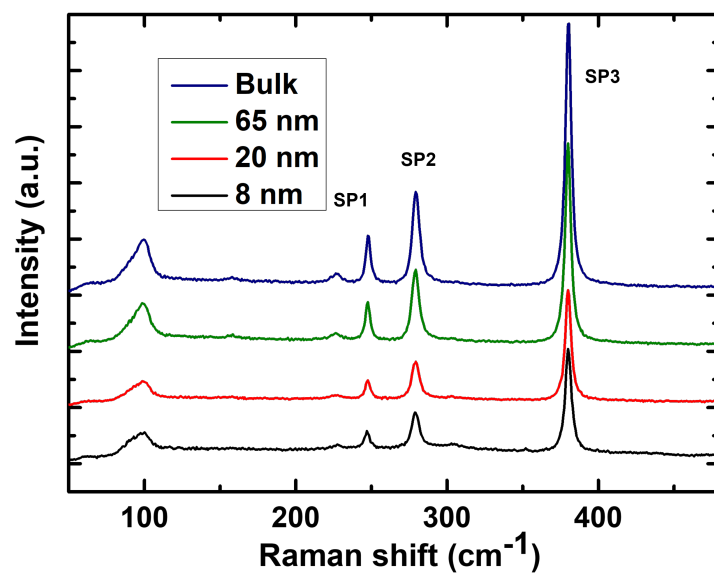


FIG. S23. Room temperature Raman spectra of FePS<sub>3</sub> with varying thickness. No significant Raman shift was observed with thickness indicating layer dependent stability of vibrational modes even in few layer FePS<sub>3</sub>.

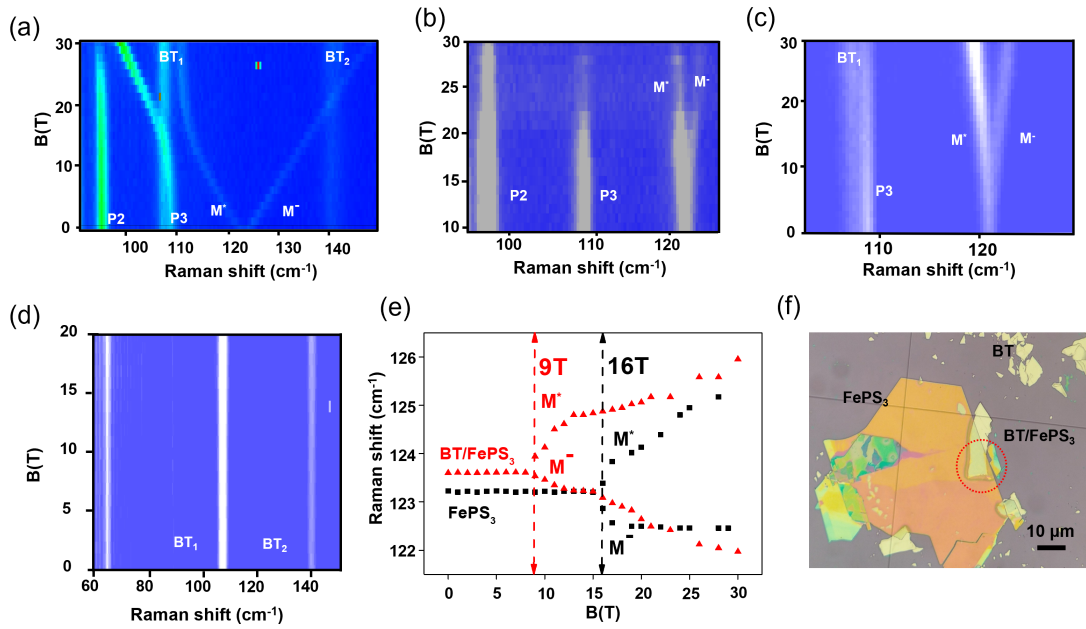


FIG. S24. (a) Evolution of the low-temperature ( $T \sim 4$  K) magneto-Raman scattering response of  $\text{Bi}_2\text{Te}_3/\text{FePS}_3$  heterostructure with magnetic field in Faraday geometry, in the spectral region from 80 to  $140 \text{ cm}^{-1}$ .  $E_g^2$  and  $A_{1g}^2$  phonon modes of  $\text{Bi}_2\text{Te}_3$  are designated as  $\text{BT}_1$  and  $\text{BT}_2$  respectively. Phonon modes ( $\text{BT}_1$ ,  $\text{BT}_2$ ) of both  $\text{Bi}_2\text{Te}_3$  and  $\text{FePS}_3$  (P2, P3, Magnon (M)) are visible in the colour map. The magnon mode at  $120 \text{ cm}^{-1}$  splits into two components  $M^*$  and  $M^-$  at/around 1 T. (b) Raman modes of  $\text{FePS}_3$  with magnetic field in Voigt configuration at  $T \sim 4$  K. The magnon mode splits at/around 16 T. (c) Raman modes of  $\text{Bi}_2\text{Te}_3/\text{FePS}_3$  heterostructure with magnetic field in Voigt configuration at  $T \sim 4$  K. The magnon mode in  $\text{FePS}_3$  splits at lower field ( $\sim 9$  T) compared to isolated  $\text{FePS}_3$ . (d) No magnetic field dependence was observed in the phonon modes of  $\text{Bi}_2\text{Te}_3$ . (e) Magnon frequency was plotted with magnetic field for both isolated  $\text{FePS}_3$  and  $\text{Bi}_2\text{Te}_3/\text{FePS}_3$  heterostructures in Voigt geometry. The magnon splitting occurs much lower field ( $\sim 9$  T) in heterostructure compared to splitting field in isolated  $\text{FePS}_3$  ( $\sim 16$  T) (f) Optical microscopy image of  $\text{Bi}_2\text{Te}_3/\text{FePS}_3$  heterostructure. High magnetic field Raman spectroscopy was performed in this heterostructure. The area marked with dotted red circle indicates the heterostructure region.

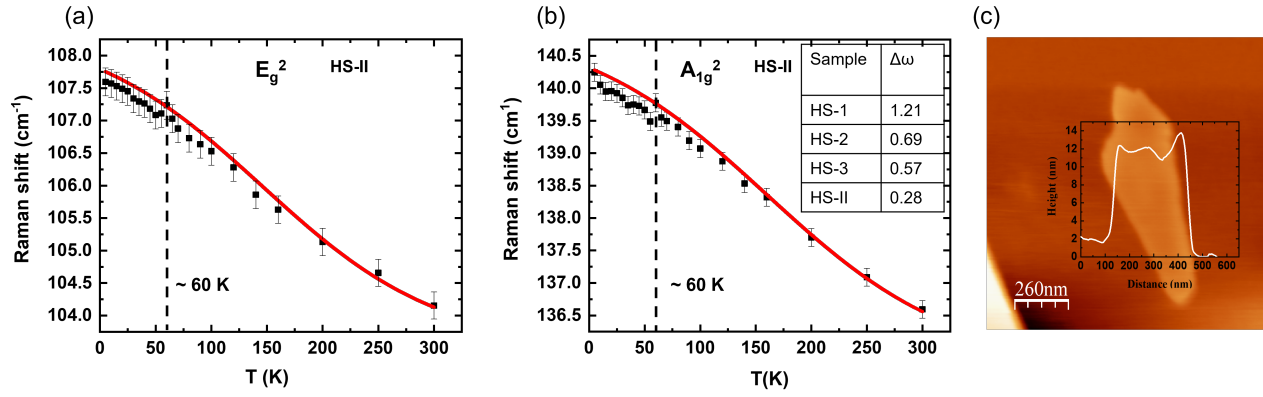


FIG. S25. Temperature dependent Raman modes of Bi<sub>2</sub>Te<sub>3</sub> in HS-II. (a) In-plane ( $E_g^2$ ) phonon mode; (b) out-of-plane ( $A_{1g}^2$ ) phonon mode. Inset of figure (b) shows the reduction of  $\Delta\omega$  with heterostructure thickness. HS (1-3) was already mentioned in the manuscript. HS-II is freshly prepared heterostructure. (c) Atomic force microscopy (AFM) image of thinner Bi<sub>2</sub>Te<sub>3</sub> used in fabricating new heterostructures (HS-I, HS-II). The thickness of the flake is  $\sim 12$  nm confirmed by the height profile.

| Bi <sub>2</sub> Te <sub>3</sub> |                                |                                  |
|---------------------------------|--------------------------------|----------------------------------|
| Raman Modes                     | $\omega(cm^{-1})(\text{Expt})$ | $\omega(cm^{-1})(\text{Theory})$ |
| $E_g$                           | -                              | 36                               |
| $A_{1g}$                        | -                              | 54                               |
| $E_g$                           | <b>106</b>                     | <b>104</b>                       |
| $A_{1g}$                        | <b>138</b>                     | <b>138</b>                       |

TABLE I. Irreducible representations of the Raman-active modes of bulk Bi<sub>2</sub>Te<sub>3</sub>. Only the high frequency  $E_g$  and  $A_{1g}$  modes are observed in experiments (second column).

| FePS <sub>3</sub> |                                  |                              |                              |
|-------------------|----------------------------------|------------------------------|------------------------------|
| Raman Modes       | $\omega(cm^{-1})(\text{zigzag})$ | $\omega(cm^{-1})(\text{FM})$ | $\Delta_{\lambda}^{rel}(\%)$ |
| B <sub>g</sub>    | 97                               | 95                           | -2.46                        |
| A <sub>g</sub>    | <b>115</b>                       | <b>102</b>                   | -11.56                       |
| A <sub>g</sub>    | <b>141</b>                       | <b>137</b>                   | -2.97                        |
| B <sub>g</sub>    | 140                              | 146                          | 3.71                         |
| B <sub>g</sub>    | 203                              | 205                          | 0.74                         |
| A <sub>g</sub>    | 208                              | 211                          | 1.73                         |
| B <sub>g</sub>    | 214                              | 214                          | 0.09                         |
| A <sub>g</sub>    | 225                              | 230                          | 2.31                         |
| B <sub>g</sub>    | 256                              | 259                          | 0.90                         |
| A <sub>g</sub>    | 268                              | 268                          | 0.04                         |
| A <sub>g</sub>    | 356                              | 359                          | 0.84                         |
| A <sub>g</sub>    | 536                              | 538                          | 0.32                         |
| B <sub>g</sub>    | 529                              | 529                          | 0.04                         |
| A <sub>g</sub>    | 546                              | 547                          | 0.18                         |

TABLE II. Irreducible representations of the Raman-active modes of FePS<sub>3</sub>. Phonon frequencies are calculated for zig-zag AFM (z-AFM) and FM spin configurations. Relative angular frequency shift ( $\Delta_{\lambda}^{rel} = \frac{\omega_{FM} - \omega_{z-AFM}}{\omega_{z-AFM}} \times 100\%$ ) due to change in the magnetic ordering of the Raman-active modes is given in the last column.

| Type of samples/<br>heterostructure  | Experimental Techniques   | Remarks  |
|--|---|--|
| Cr-doped (Bi,Sb) <sub>2</sub> Te <sub>3</sub> (BST) film                         | Quantum transport measurements<br>[Quantum anomalous Hall effect<br>(QAHE)] | Magnetic doping introduces detrimental effects leading to a very low operational temperature 30K<br><b>(Science 2013, 340, 167.)</b>             |
| V-doped BST film   | Quantum transport measurements<br>(QAHE)                                    | Operational temperature was slightly increasing that was at around 120 mK<br><b>(Nat. Mater. 2015, 14, 473)</b>                                  |
| Modulation-doped [Cr:BST/BST] pentalayer heterostructure                         | Quantum transport measurements<br>(QAHE)                                    | There was slight improvement of the zero field QAHE temperature (2K)<br><b>(Nat. Mater. 2015, 14, 473; Appl. Phys. Lett. 2015, 107, 182401.)</b> |
| Proximity coupled BST films/TIG  | Transport Measurement (AHE)   | AHE observed at 400 K <b>(Sci. Adv. 2017, 3, e1700307.)</b>  |
| Co-doped (Cr,V):BST film   | Quantum transport measurements<br>(QAHE)                                    | QAHE temperature 1.5 K. <b>(Adv. Mater. 2018, 30, 1703062.)</b>  |
| Proximity-coupled (Zn, Cr) Te/BST/(Zn,Cr)Te heterostructures                     | Quantum transport measurements<br>(QAHE)                                    | QAHE temperature 1.5 K. <b>(Appl. Phys. Lett. 2019, 115, 102403.)</b>  |
| MnBi <sub>2</sub> Te <sub>4</sub> /Bi <sub>2</sub> Te <sub>3</sub> superlattices | Quantum transport measurements<br>(QAHE)                                    | QAHE temperature 7 K. <b>(Nat. Phys. 2021, 17, 36.)</b>  |
| Bi <sub>2</sub> Se <sub>3</sub> /Y <sub>3</sub> Fe <sub>5</sub> O <sub>12</sub>  | Magneto-optic Kerr effect (MOKE)  | Indicate domain wall of flipping spins<br><b>(Nano Lett. 2014, 14, 3459.)</b>  |
| EuS/Bi <sub>2</sub> Se <sub>3</sub>  | Magnetic second-harmonic generation   | Investigation of in-plane and out-of-plane ferromagnetic moments <b>(Nat. Commun. 2016, 7, 12014.)</b>   |
| EuS/Bi <sub>2</sub> Se <sub>3</sub> and EuS/BST                                  | X-ray Magnetic Circular Dichroism   | Challenges the claims of <b>Nat. Commun. 2016, 7, 12014 (Phys. Rev. Lett. 2020, 125, 226801.)</b>  |
| EuS/Bi <sub>2</sub> Se <sub>3</sub>  | PNR measurements  | Magnetic moments are canted at the interface <b>(Nature 2016, 533, 513.)</b>   |
| Bi <sub>2</sub> Te <sub>3</sub> /FePS <sub>3</sub>                               | Raman spectroscopy  | Proximity induced Spin phonon coupling in Bi <sub>2</sub> Te <sub>3</sub> ; Reduction of Néel Temperature <b>(Current study)</b>                 |

TABLE III. Performance comparisons of different Topological Insulator heterostructures using various experimental techniques

| Modes           | $\omega$ (cm <sup>-1</sup> ) (Bulk) | $\omega$ (cm <sup>-1</sup> ) (Monolayer) |
|-----------------|-------------------------------------|--|
| E <sub>g</sub>  | 36                                  | 36                                       |
| A <sub>1g</sub> | 54                                  | 53                                       |
| E <sub>g</sub>  | 104                                 | 104                                      |
| A <sub>1g</sub> | 138                                 | 142                                      |

TABLE IV. Irreducible representations of the Raman-active modes of bulk and single layer Bi<sub>2</sub>Te<sub>3</sub>.

| System  | $E_1^{AFM}$ (Fig S7a)<br>(eV) | $E_2^{FM}$ (Fig S7b)<br>(eV) | $J_{AFM} = \frac{(E_2^{FM} - E_1^{AFM})}{4S^2}$<br>(meV) | $T_N$ (K) |
|---|-------------------------------|------------------------------|--|-----------|
| FePS <sub>3</sub> Monolayer (expt.)                                   | -102.180                      | -102.029                     | 9.44   | 110       |
| FePS <sub>3</sub> Monolayer<br>(-0.5 % strain)                        | -103.834                      | -103.724                     | 6.88   | 80        |
| Bi <sub>2</sub> Te <sub>3</sub> /FePS <sub>3</sub><br>Heterostructure | -174.935                      | -174.839                     | 5.96   | 69        |

TABLE V. Calculation of AFM exchange in FePS<sub>3</sub> monolayer with and without strain, and within the heterostructure setup involving Bi<sub>2</sub>Te<sub>3</sub>.

| Thickness of FePS <sub>3</sub> | Raman Mode<br>(Peak position in cm <sup>-1</sup> ) |        |        | Remarks  |
|--------------------------------|--|--------|--------|--|
|                                | SP1  | SP2    | SP3    |  |
| 8 nm                           | 247.08   | 279.17 | 380.19 | No significant Raman shift was observed with thickness of FePS <sub>3</sub> from bulk to few layer |
| 20 nm                          | 247.56   | 279.23 | 380.08 |  |
| 45 nm                          | 247.72   | 279.40 | 380.16 |  |
| 65 nm                          | 247.53   | 279.13 | 380.01 |  |
| Bulk                           | 247.86   | 279.47 | 380.23 |  |

TABLE VI. The frequencies of FePS<sub>3</sub> spin-phonon (SP) coupled modes are presented with varying thickness (Figure S23). No significant Raman shift was observed with the thickness of FePS<sub>3</sub>.



|   | Thickness                | Raman Mode of Bi <sub>2</sub> Te <sub>3</sub> (Peak position in cm <sup>-1</sup> ) |                              | Reference                               | Remarks   |
|---|--------------------------|--|------------------------------|---|---|
|   |                          | E <sub>g</sub> <sup>2</sup>  | A <sub>1g</sub> <sup>2</sup> |   |   |
| Bi <sub>2</sub> Te <sub>3</sub><br>(Ar <sup>+</sup> laser)      |                          | E <sub>g</sub> <sup>2</sup>  | A <sub>1g</sub> <sup>2</sup> | Nano Research 2013, 6(9): 688–692       | <input type="checkbox"/> In-plane Raman mode (E <sub>g</sub> <sup>2</sup> ) barely shows frequency shift with the thickness.<br><input type="checkbox"/> Out-of-plane Raman mode (A <sub>1g</sub> <sup>2</sup> ) exhibits a frequency shift ~ (6-7) cm <sup>-1</sup> when reducing the thickness.   |
|   | 1 QL                     | 102  | 141                          |   |   |
|   | 2 QL                     | 102  | 135                          |   |   |
|   | 7 QL                     | 102  | 134                          |   |   |
|   | 40 QL                    | 102  | 135                          |   |   |
|   | Bulk                     | 102.3  | 134                          |   |   |
|   |                          |  |                              |   |   |
| Bi <sub>2</sub> Te <sub>3</sub><br>Thin film<br>(488 nm)        | 10 nm                    | 101.4  | 132.9                        | J. Appl. Phys. 111, 054305 (2012)       |   |
|   | 50 nm                    | 101.5  | 132.39                       |   |   |
| Bi <sub>2</sub> Te <sub>3</sub><br>Nanostructure<br>(633 nm)    | 12 QL<br>(Nanosheet)     | 98   | 140                          | Applied Surface Science 457(2018) 41-48 | <input type="checkbox"/> Phonon modes of Bi <sub>2</sub> Te <sub>3</sub> changes depending on the structure whether it is nanosheets or nanoplatelets.  |
|   | 12 QL<br>(Nanoplatelets) | 99   | 127                          |   |   |
| Bi <sub>2</sub> Te <sub>3</sub> crystal<br>and film<br>(488 nm) | 4 nm                     | 101.4  | 132.9                        | Appl. Phys. Lett. 96, 153103 (2010)     | <input type="checkbox"/> In-plane Raman mode (E <sub>g</sub> <sup>2</sup> ) does not show significant frequency shift with the thickness.<br><input type="checkbox"/> Out-of-plane Raman mode (A <sub>1g</sub> <sup>2</sup> ) exhibits a frequency shift when reducing the thickness.   |
|   | 40 nm                    | 101.3  | 133.0                        |   |   |
|   | Bulk                     | 101.7  | 134.0                        |   |   |
| Bi <sub>2</sub> Te <sub>3</sub>                                 | Bulk                     | 104.0  | 138.0                        | Our work (Theory)                       | <input type="checkbox"/> Out-of-plane vibration mode shows frequency shift (~ 4 cm <sup>-1</sup> ) with thickness whereas in-plane phonon mode remains almost unchanged in frequency from bulk to monolayer.<br><input type="checkbox"/> Phonon frequencies and the point group symmetry (D3d) remain invariant, irrespective of thickness. |
|   | Monolayer                | 104.0  | 142.0                        |   |   |

TABLE VII. Thickness dependent Raman shift of Bi<sub>2</sub>Te<sub>3</sub> with different structural form and wavelength excitation. No significant Raman shift was observed in E<sub>g</sub><sup>2</sup> mode and a prominent shift (~ 6 cm<sup>-1</sup>) was observed in A<sub>1g</sub><sup>2</sup> mode with thickness.

| Laser excitation (nm) | Thickness   | Phonon dynamics (Peak Position)  | Reference   | Remarks   |
|-----------------------|---|--|---|---|
| 647.1                 | Dropcasted Bi <sub>2</sub> Te <sub>3</sub> Nanoflakes (~15 nm)  | Anharmonic in the temperature window (3 K to 295 K)  | Sören Buchenau <i>et al.</i> , Phys. Rev. B 101, 245431 (2020)                | Bi <sub>2</sub> Te <sub>3</sub> shows no phonon anomaly in frequency in the whole temperature window. It's a pure phonon-phonon coupling phenomena irrespective of thickness and laser wavelength excitation.   |
| 532                   | Bi <sub>2</sub> Te <sub>3</sub> Single crystal (~135 μm)  | Anharmonic in the temperature window (93K-298K)  | Priyanath Mal <i>et al.</i> Phys. Chem. Chem. Phys., 2019, 21, 15030          |   |
| 632                   | Mechanically exfoliated Bi <sub>2</sub> Te <sub>3</sub> (20 nm & 60 nm)                                 | Anharmonic in the temperature window (153 K to 303 K)  | Manavendra P. Singh <i>et al.</i> , Current Chinese Science, 2021, 1, 453-459 |   |
| 533                   | Bi <sub>2</sub> Te <sub>3</sub> Bulk film (~4 μm)   | Linearly vary with temperature in the high temperature window (243 K to 573 K)   | Duanhui Li <i>et al.</i> , Phys. Status Solidi RRL 6, No. 6, 268–270 (2012)   | Bi <sub>2</sub> Te <sub>3</sub> shows no phonon anomaly in frequency and varies linearly in the high temperature window. (phonon-phonon coupling)   |
| 633                   | Bi <sub>2</sub> Te <sub>3</sub> Nanowire and nanoribbon   | Linearly vary with temperature in the high temperature window (243 K to 573 K)   | Dambi Park <i>et al.</i> , Scientific Reports 6, 19132 (2016)                 |   |
| 473                   | Exfoliated bulk Bi <sub>2</sub> Te <sub>3</sub> flake (~140 nm, ~250 nm, >500 nm)                       | Anharmonic in the temperature window (5 K-300 K)   | Our work  | 1. Bi <sub>2</sub> Te <sub>3</sub> (named as 'Isolated Bi <sub>2</sub> Te <sub>3</sub> ' in the manuscript) shows no phonon anomaly in frequency in the whole temperature window.<br>2. Bi <sub>2</sub> Te <sub>3</sub> shows phonon anomaly in frequency (spin-phonon coupling) at/around 60 K due to FePS <sub>3</sub> . Strength of spin-phonon coupling (Δω) reduces with thickness of individual material in the Bi <sub>2</sub> Te <sub>3</sub> /FePS <sub>3</sub> heterostructure without affecting the characteristic temperature for spin-phonon coupling (~60K).<br>3. Bi <sub>2</sub> Te <sub>3</sub> recover the anharmonicity when a hexagonal boron nitride (independent of thickness) is placed in between bulk Bi <sub>2</sub> Te <sub>3</sub> and bulk FePS <sub>3</sub> . |
|                       | Bulk Bi <sub>2</sub> Te <sub>3</sub> (>500 nm)/ Bulk FePS <sub>3</sub> (~150 nm)                        | Deviation from anharmonicity at/around 60 K in Bi <sub>2</sub> Te <sub>3</sub> (Spin-phonon coupling)  |   |   |
|                       | Bulk Bi <sub>2</sub> Te <sub>3</sub> (~250 nm)/ Bulk FePS <sub>3</sub> (~88 nm)                         | Deviation from anharmonicity at/around 60 K in Bi <sub>2</sub> Te <sub>3</sub> (Spin-phonon coupling) Strength of coupling reduces.                        |   |   |
|                       | Bulk Bi <sub>2</sub> Te <sub>3</sub> (~140 nm)/ Bulk FePS <sub>3</sub> (~10 nm)                         | Deviation from anharmonicity at/around 60 K in Bi <sub>2</sub> Te <sub>3</sub> (Spin-phonon coupling). More reduction of strength of spin-phonon coupling. |   |   |
|                       | Bulk Bi <sub>2</sub> Te <sub>3</sub> (>500 nm) /Bulk hBN (>100 nm)/Bulk FePS <sub>3</sub> (~150 nm)     | Anharmonic in the temperature window (5 K-300K).   |   |   |
|                       | Bulk Bi <sub>2</sub> Te <sub>3</sub> (>500 nm) /few layer hBN (~10 nm)/Bulk FePS <sub>3</sub> (~150 nm) | Anharmonic in the temperature window (5 K-300K).   |   |   |

TABLE VIII. Phonon dynamics of Bi<sub>2</sub>Te<sub>3</sub> with temperature for a fixed thickness of Bi<sub>2</sub>Te<sub>3</sub>. Bi<sub>2</sub>Te<sub>3</sub> shows no phonon anomaly in frequency with temperature irrespective of thickness, wavelength excitation and different form of Bi<sub>2</sub>Te<sub>3</sub>. It is pure phonon-phonon coupling.

| Structure                                 | Configuration | Magnon splitting field (Tesla) |
|---|---------------|--------------------------------|
| FePS <sub>3</sub>                         | Faraday       | 1                              |
|   | Voigt         | 16                             |
| BT  | Faraday       | No magnetic field dependency   |
|   | Voigt         | No magnetic field dependency   |
| BT/FePS <sub>3</sub><br>(Heterostructure) | Faraday       | 1                              |
|   | Voigt         | 9                              |

TABLE IX. Magnon splitting field in FePS<sub>3</sub>, Bi<sub>2</sub>Te<sub>3</sub> and Bi<sub>2</sub>Te<sub>3</sub>/FePS<sub>3</sub> heterostructures in different magnetic field configurations.